Study of the imine hydrogenation mechanism over an Ir-based catalyst using DFT

Britt van Dongen

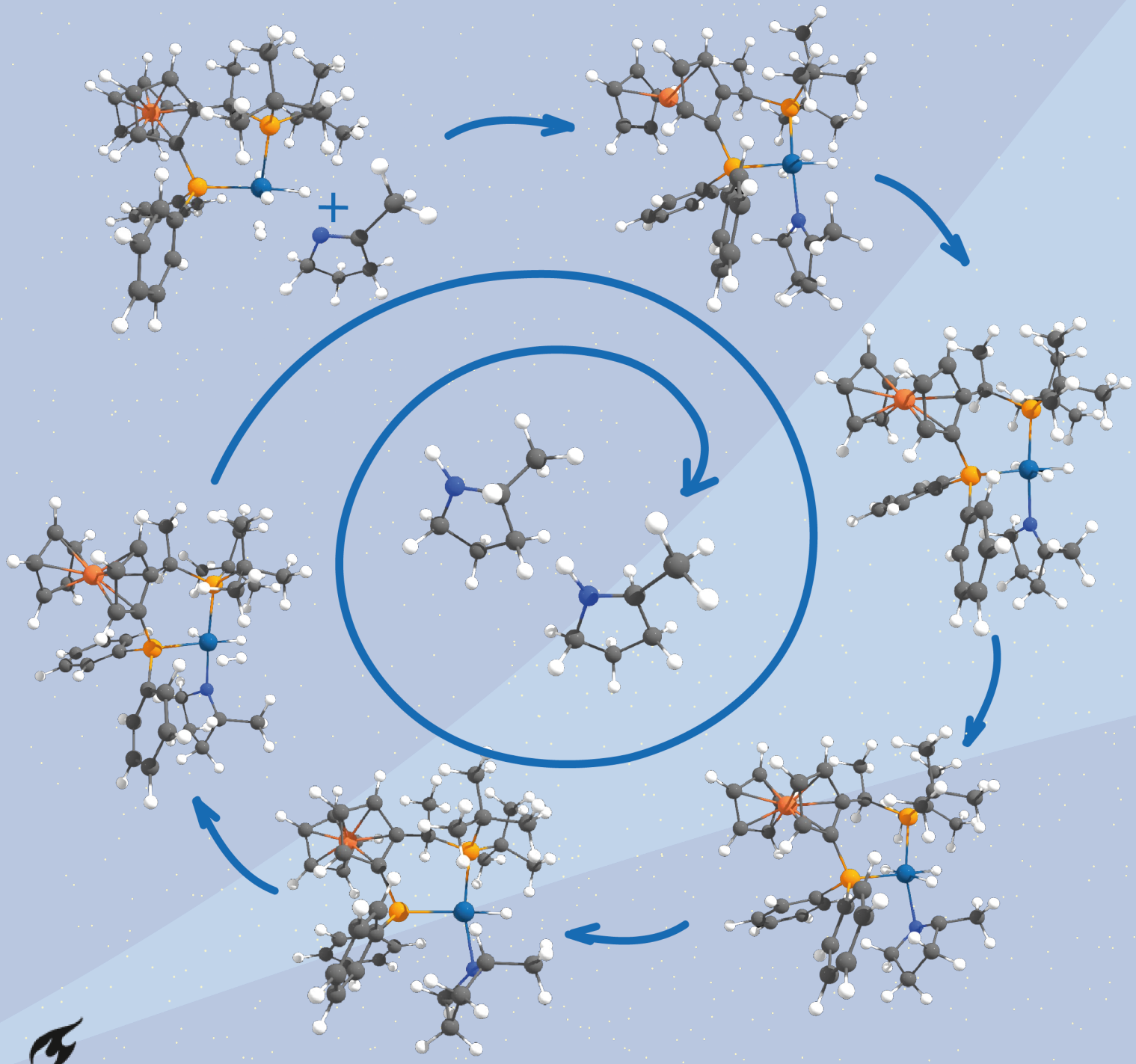

TU Delft

Study of the imine hydrogenation mechanism over an Ir-based catalyst using DFT

by

Britt van Dongen

to obtain the degree of Bachelor of Science
at the Delft University of Technology,
to be defended publicly on Friday June 24, 2022 at 10:00 AM.

Performed at:
Inorganic Systems Engineering
Department of Chemical Engineering
Faculty of Applied Sciences

Under supervision of:
Prof. Dr. E.A.Pidko
MSc. A.V. Kalikadien

Student number:	5186781/s2606054	
Project duration:	April 19, 2022 – June 24, 2022	
Thesis committee:	Prof. Dr. E. A. Pidko,	TU Delft, supervisor
	Prof. Dr. F. C. Grozema,	TU Delft

TU Delft Delft University of Technology

ISEgroup ChemE @ TU Delft

Abstract

The search for better catalysts for imine hydrogenation is an ongoing challenge. Understanding of the underlying mechanism can play an important role in the evolution of catalyst design. The goal of this research is to get more insight in the asymmetric hydrogenation (AH) of 2-Methyl-1-pyrroline with an Ir-based catalyst with a phosphorous bidentate ligand (JosiPhos) using density functional theory (DFT) calculations. In this research, two mechanisms are investigated. The inner sphere C-migration mechanism is explored for all possible options for the coordination of the substrate to the catalyst complex. A conformer search with Conformer–Rotamer Ensemble Sampling Tool (CREST) is done on three transition states (TS) to investigate if ensemble representations are important for the determination of the enantioselectivity of a certain path. The outer sphere mechanism is only partially explored. Using DFT, the energy landscape of each reaction path could be mapped out.

Of the inner sphere C-migration mechanism, ten possible reaction paths were obtained. The two most thermodynamically favourable paths are the paths where the substrate binds on one specific equatorial coordination site. There is no substantial preference for the formation of one enantiomer over the other. However, CREST calculations generated possible conformers of certain transition states, some with a lower energy. This resulted in a preference for the formation of the R-enantiomer for the inner sphere C-migration mechanism.

Little can be said about the outer sphere mechanism since there is not enough data yet to form a clear conclusion about the favourability of this mechanism. One of the findings was that another type of outer sphere mechanism was found other than the outer sphere mechanism proposed based on literature. To be able to state what mechanism is the most likely to occur, more quantitative research is needed on the outer sphere mechanism and other possible mechanisms.

Contents

Abbreviations and acronyms

AH	Asymmetric Hydrogenation
ATH	Asymmetric Transfer Hydrogenation
B_e	rotational constant
CRE	Conformer/Rotamer Ensemble
CREST	Conformer–Rotamer Ensemble Sampling Tool
DCM	Dichloromethane
DFT	Density Functional Theory
e.e.	enantiomeric excess
E	Electronic energy
G	Gibbs free energy
GC	Genetic Crossing
GGA	Generalized Gradient Approximation
H	Enthalpy
HF	Hartree Fock
HK	Hohenberg-Kohn
ISE	Inorganic System Engineering
KS	Kohn-Sham
LDA	Local-Density Approximation
MTD	Meta-dynamic
PES	Potential Energy Surface
Ph	Phenyl
pK_a	acidity constant
QM	Quantum mechanical
RMSD	Root Mean Square Deviation
SE	Schrödinger equation
t-Bu	tert-Butyl
TS	Transition state

1

Introduction

Catalysts are used in many industrial processes and a lot of research is done to develop catalysts with the right catalytic properties to improve the efficiency of the process. One of those industrial processes is the synthesis of chiral amines. A specific example which shows the importance of enantioselective imine hydrogenation is the Metolachlor process. It is the largest enantioselective catalytic process with a production of quantities of more than 10.000 tonnes per year. (S)-Metolachlor is one of the most important grass herbicides for use in maize [1]. Multiple Ir-based catalytic systems used to produce the chiral herbicide (S)-Metolachlor provided enantioselectivity of 79% or even higher [1, 2].

A catalyst can be defined as a substance which increases the rate at which a chemical reaction approaches equilibrium without becoming itself permanently involved [3, 4]. It provides an alternative pathway for making and breaking of bonds. This pathway has a lower activation energy than that required for the uncatalysed reaction. Catalysts are divided in three main categories: homogeneous, heterogeneous and biocatalysts [5].

Heterogeneous catalysts are in a different aggregation state than the reactants. Often, they are solid materials, for instance metal nanoparticles. They speed up the reaction between gaseous and liquid reactants or reactants dissolved in a liquid. It is beneficial to disperse the solid particles on a support material to increase the number of active sites [5].

Homogeneous catalysts are in the same aggregation state as the reactants, typically the liquid phase [5]. Although biocatalysts also fall under this definition, they are considered to be a distinct type of catalyst and generally are called enzymes. For the homogeneous catalysts, only organometallic compounds are discussed. These organometallic compounds consists of a (transition) metal centre and ligands. A lot of research has already been done in the field of homogeneous catalysis. Nevertheless, it remains a challenge to find the optimal combination and geometry of a metal and its ligands to obtain high efficiencies for certain chemical reactions. This report will describe a specific reaction, namely asymmetric imine hydrogenation, which is catalysed by a homogeneous catalyst.

Imine hydrogenation is an important reaction because the formed product, a chiral amine, is widely used as a building block in fine chemical, agrochemical and pharmaceutical industries [6–8]. Stereochemistry is a dominant concept in this field of work. Stereoisomers are compounds which share identical molecular formulas, but differ in their three-dimensional arrangement. Due to the chirality of a molecule (in this case a chiral amine), two enantiomers can be distinguished. Enantiomers are stereoisomers which are nonsuperimposable mirror images. These chiral molecules contain an asymmetric point, often a carbon atom with four different substituents [9].

There are two used methods to produce chiral amines: asymmetric hydrogenation (AH) and asymmetric transfer hydrogenation (ATH). For the first reaction molecular hydrogen is used as hydrogen source and for the second reaction small organic molecules like 2-propanol are used as hydrogen source [8]. There are multiple catalysts with chiral organic ligands reported which could facilitate the hydrogenation of the C=N double bond. These catalysts are based on for example iridium, rhodium, ruthenium, titanium and palladium. Iridium-based catalysts are the most widely studied and outstanding catalysts used for AH [8]. Compared to other transition metal based catalysts, they provide high activities and enantioselectivities under mild conditions [7].

For industries, it is of great importance to obtain enantiopure compounds and thus get a high enantiomeric excess (e.e.), which is defined as the excess of the major enantiomer over the other [10]. The impor-

tance of pure enantiomers is clearly seen in the pharmaceutical industry because the physiochemical and biochemical properties of racemic mixtures and individual stereoisomers can differ significantly [9]. Some drugs are prescribed as a racemic mixture, whereof only one enantiomer has the main therapeutic effect while the other one may produce adverse effects. These adverse effects range from inactive and qualitatively effects to greater toxicity [11]. In recent years, a lot of research has been done to achieve the most enantioselective catalysts and to get in grips with stereocontrol. In general, the enantioselectivity is determined by the relative rates of the competing enantioselective paths [6]. This is difficult to control and depends on many factors. An overview of four factors will be given.

One of those factors is the structure of the ligands since they control the outcome of the enantiomeric product by steric and electronic factors. The (imine) substrate is also of importance to the selectivity because bulky and flexible substituents generally give lower enantioselectivities. Moreover, strongly coordinated solvents and additives can also reduce the enantioselectivity significantly by possible blocking of a contact point between the metal and the substrate. Another factor is the potential E/Z isomerization of the substrate since they interact differently with the catalyst [6].

The search for better catalysts is a challenge which involves trial-and-error approaches in the laboratory. The factors influencing the enantioselectivity as well as the knowledge gap in the underlying mechanisms play important parts in this challenge [8]. To get more insight in the underlying mechanisms, computational calculations can be performed. The majority of the studies uses density functional theory (DFT) [12]. DFT can be used for structure optimization, reaction mechanism exploration and to get spectral signatures of molecules [13].

In literature, DFT calculations on multiple reaction mechanisms for imine hydrogenation are presented. The mechanistic proposals can be divided into two main classes: inner and outer sphere mechanisms. In multiple studies the outer sphere mechanism is proven to be the most thermodynamically favourable path for acyclic imine hydrogenation [6, 8]. During this mechanism, the hydrogenation of the substrate (imine) occurs partially in the outer shell. During inner sphere hydrogenation, the imine is bound to the transition metal of the catalyst at all times [8].

However, there appears to be a research gap: AH of cyclic imines is less explored than their acyclic analogue [7]. Therefore, this report will focus on multiple reaction paths of the AH of the cyclic imine substrate: 2-Methyl-1-pyrroline. The aim of this research is to get more insight in the AH reaction of 2-Methyl-1-pyrroline with an Ir-based catalyst with a phosphorous bidentate ligand (JosiPhos) using DFT calculations. Two different mechanisms will be explored: an outer sphere mechanism and inner-sphere C-migration mechanism. The construction of the mechanisms is based on previously proposed mechanisms for acyclic imine hydrogenation with an iridium-based catalyst [6]. The constructed outer and inner sphere mechanisms will be compared to each other to see which one is thermodynamically more favourable and thus more likely to occur. For the inner sphere C-migration mechanism, possible conformers will be found of the transition states (TS) of three paths with a Conformer–Rotamer Ensemble Sampling Tool (CREST). This will be done to investigate if there are conformers which are lower in energy that influence the favourability of a certain path. The difference in geometry will be quantitatively described with the Root-mean square deviation (RMSD).

The report is structured in the following way. First, the theoretical background about the computational methods used in this research is given. Herein, the density functional theory (DFT), the Conformer-Rotamer Ensemble Sampling Tool (CREST) and the Root-mean square deviation (RMSD) will be discussed. Thereafter, the results of this research are presented. Finally, a conclusion and an outlook on future research is given.

2

Computational methods

In this chapter the computational methods which are used in this research are explained. First, the density functional theory (DFT) will be described, because this is the main used method. Thereafter, the Conformer–Rotamer Ensemble Sampling Tool (CREST) will be explained. Lastly, the root-mean-square deviation (RMSD) will be described.

2.1. Density Functional Theory

In this research, DFT is used as the quantum mechanical (QM) calculation method, since DFT can be conducted by chemists on common desktop computers with user-friendly software [12, 13]. Nowadays, DFT is used to get information about geometric, electronic and spectroscopic properties of atoms or molecules. This method allows structures to be optimized and reaction mechanisms to be explored [13–15]. Some might say that it is revolutionary in the quantum chemistry [15]. The main benefit of using DFT is the computational efficiency and accuracy in quantitative calculations of molecules and its properties at much lower costs than traditional ab initio wave function techniques; it thus has a good quality/cost ratio [15, 16]. To understand how the DFT method is established, a description of the Schrödinger equation needs to be given first. This is done in subsection 2.1.1.

2.1.1. Schrödinger equation

The Schrödinger equation (SE) describes the quantum nature of matter [17] and is given by the following equation:

$$\hat{H}\Psi = E\Psi \tag{2.1}$$

Ψ is called the wavefunction of the system. The square of the absolute value of the wavefunction gives the probability density which represents the probability of finding an electron at some given point in space. $\hat{H}$ is the Hamiltonian operator for a system containing N electrons and M nuclei and is given in Figure 2.1.

Kinetic energy Potential energy

$$\boldsymbol{H} = \underbrace{-\frac{1}{2}\sum_{i=1}^{N}\nabla_i^2}_{\text{Electrons}} \underbrace{-\frac{1}{2}\sum_{i=1}^{N}\frac{\nabla_i^2}{M_A}}_{\text{Nuclei}} \underbrace{-\sum_{i=1}^{N}\sum_{A\neq 1}^{M}\frac{Z_A}{r_{iA}}}_{\substack{\text{Coulomb attraction}\\ \text{(nucleus-electron)}}} + \underbrace{\sum_{i=1}^{N}\sum_{j\neq 1}^{M}r_{ij}^{-1}}_{\substack{\text{Coulomb repulsion}\\ \text{(electron-electron)}}} + \underbrace{\sum_{A=1}^{M}\sum_{A'>A}^{M}\frac{Z_{A'}Z_A}{R_{AA'}}}_{\substack{\text{Coulomb repulsion}\\ \text{(nucleus-nucleus)}}}$$

Figure 2.1: Non-relativistic Hamiltonian operator in the time-independent schrödinger equation [18].

When the Hamiltonian operates on the wavefunction, the total energy (kinetic and potential) of the system can be derived. In the equation, indices i and A/A' run over the electrons and nuclei respectively. Z_A stands for the charge of nucleus A and r_{ij} stands denotes the distance between electron i and electron j. Furthermore, r_{iA} stands for the distance between nucleus A and the ith electron and $R_{AA'}$ stands for the internuclear distance.

There are multiple approaches to solve the Schrödinger equation which involve the Hartree Fock (HF), the Hohenberg-Kohn (HK) and the Kohn-Sham (KS) theorems. However, before the wavefunctions and the

energy of the system are determined, an assumption must be made which will simplify the Hamiltonian. It is assumed that the kinetic energy of the nuclei is zero and that the nucleus-nucleus repulsion is a constant term. These approximations can be made because nuclei are far more heavier than electrons and move relatively much slower. This approximation is called: The Born Oppenheimer approximation [19]. Now, the approaches to solve the SE will be discussed.

The Hartree Fock theorem assumes that the wavefunction of the system can be approximated by a single Slater determinant of N spin orbitals. The main shortcoming of the HF method is that it neglects the electron correlations [14]. The Hohenberg-Kohn method makes use of the electron density. It states that the ground-state electron density determines the electronic wavefunctions and that the energy of an electron can be described as a functional of the electron density. This functional is a minimum for the ground-state density [14, 17].

The theorem that is used nowadays in DFT is called the Kohn-Sham theorem. The KS method can be seen as a variant of the HK method, since the basis is a noninteracting system yielding the same density as the original problem. The wavefunctions can be presented in a Slater determinant and can be solved in a simple way. However, the exact solution can only be found when the exchange-correlation functionals are known. This is only the case for the free electron gas [14]. Nevertheless, approximations exist which give certain levels of accuracy. Now, an overview of some exchange-correlation functionals is given in subsection 2.1.2.

2.1.2. Exchange-correlation functionals

Exchange-correlation functionals use electron density to describe the many-body effects within a single particle formalism [17]. In this subsection, four approximations of exchange-correlation functionals are briefly described: local-density approximation (LDA), generalized gradient approximation (GGA), meta-GGA and hybrid functionals.

LDA is the simplest approximation and states that the energy of a system only depends on the density at the point where the functional is evaluated. It gives good geometries, but it has a strong tendency for overbinding [14, 17].

GGA is an improvement compared to LDA because it not only includes the electron density but also the gradient. Therefore, it gives a better description of the inhomogeneity of a molecular structure [14, 20]. Examples of GGA functionals are BP86 and PBE. Their accuracy is good enough for structural parameters, but the results are less accurate for other properties [14]. An improvement on GGA's were the Meta-GGA which are generated by adding dependence of the local spin kinetic energy densities [20].

The most recent ones are hybrid functionals. In these functionals, a fraction of Hartree-Fock exact exchange is included in the functional [17]; it is a mix of GGA and exact HF exchange. Examples of hybrid functionals are B3LYP and PBE1PBE. B3LYP functional is the most widely used functional in chemistry today [17, 21]. However, for this research it is chosen to make use of the PBE1PBE functional. The ISE group applied this functional to transition metal structures, hence this functional is also used in this research. Furthermore, although GGA functionals provide good geometries, for certain system only high accuracy can be obtained by using hybrid functionals [14].

The accuracy of the results is determined by the choice of exchange-correlation functional as well as the choice of basis set [12]. Therefore, a description of basis sets is given in subsection 2.1.3.

2.1.3. Basis sets

A basis set is a mathematical description of the orbitals of a system. It is a linear combination of algebraic functions [22]. Basis sets have been treated as a set of building blocks which can be added to get the desired features [23]. The size of the basis set can thus differ significantly. Larger basis sets deliver more reliable results but also have a smaller computational efficiency, which is defined as the time needed to complete a calculation [12]. For the study of large transition metal complexes it is needed to find a right balance between accuracy and computational costs.

For this research it is chosen to work with the def2SVPP basis set. This set contains polarization functions for all atoms except the hydrogen atom. It describes the polarization of the electron density of the atom in the molecule [18]. For p elements it contains a polarizing d function, for d elements a diffuse p set and for s elements large polarization sets are included. The def2SVPP basis set is one of the smaller def2 sets and thus has a slightly higher error in atomization energies per atom in the DFT calculations compared to larger basis sets [24]. Nevertheless, this basis set has a sufficient enough accuracy for this research project; the structures optimized by DFT quickly converge, even with a small basis set size [14].

There are more parameters which can be added for the DFT calculations such as the type of solvent

and the corrections for the London dispersion interactions. These parameters will be described in subsection 2.1.4 and subsection 2.1.5 respectively.

2.1.4. Solvation

Solvent effects can also be included in DFT calculations. In recent decades two main techniques were developed: continuum models and discrete solvent models. In continuum models, the solvent is treated as a continuum, with a uniform dielectric constant, surrounding the solute molecule placed in a cavity [15]. In discrete solvent models, the solvent molecules are considered discreetly. This has as a result that the number of interacting particles and degrees of freedom of a system increases significantly compared to continuum models [25].

For this research, a continuum model, CPCM, is used as the solvent model. Compared to a discreet solvent model it has lower computational costs [2]. The solvent which is used in the calculations is dichloromethane (DCM). The main reason why DCM is used as the solvent is because it is used in the laboratory experiments done on these catalyst structures in the ISE group. Furthermore, it is a polar solvent which can dissolve a wide range of organic compounds [26].

2.1.5. Dispersion corrections

In the used KS method, the dispersion energy is not included. The binding energy curves of the standard functionals decay exponentially instead of $-C_6/R^6$, where R is the separation between molecules and C_6 is the van der Waals coefficient [21]. To improve the accuracy in DFT calculations, London dispersion interactions must be included. Therefore, multiple methods were developed. One of those methods is developed by Grimme. It provides an empirical correction to DFT results. Therefore, Grimme's 3D dispersion correction with BJ-damping was used in this research. The damping function has the advantage of avoiding repulsive interatomic forces at shorter distances [27].

Now that all the parameters which are chosen for this research are described, the use of DFT in this research will be covered in subsection 2.1.6.

2.1.6. Geometry optimization, energetics and reaction mechanism

In this research two possible reaction mechanisms for the hydrogenation of 2-Methyl-1-pyrroline are explored. DFT is used to do that. Transition states and optimized geometries of reactants, intermediates and end products need to be found. This is done by computing the energy and exploring the potential energy surface (PES). The transition states of the inner sphere C-migration mechanism were found by performing a scan coordinate calculation where the hydride translates to the C*-atom in steps of 0.1 angstrom. The transition state of the outer sphere mechanism was found by performing a scan coordinate calculation where the C*-H bond of the substrate is stretched in steps of 0.1 angstrom.

Local minima in the PES represent optimized geometries and saddle points represent transition states [12]. Mathematically, the extreme values of the PES are found by taking the first derivative of the Root Mean Square (RMS) gradient norm with respect to position. When this is zero, the extreme values are found. To determine if these are optimized geometries or a transition states, the second derivative of the RMS gradient norm with respect to position needs to be calculated. For (local) minima this second derivative is larger than zero and for transition states the second derivative is zero.

The frequencies that vibrations would have in an infrared spectrum also give information whether the structure is an optimized geometry or a transition state. Reactants, intermediates and end products must only display real (positive) frequencies. On the other hand, a transition state is displayed by an imaginary (negative) frequency that is associated with the motion of the atom along the bond that is formed [12].

2.2. Conformer–Rotamer Ensemble Sampling Tool (CREST)

In this research, the importance of ensemble representations of transition states is investigated. It is interesting to look if there are conformations of the transition states with a lower energy minimum. Based on the number of conformers, the corresponding energy and geometry, it will become clear if conformers of transition states play a significant role. Comparison of the energy of the conformers of the structures which generate different enantiomers will give more insight in the enantioselectivity and thus the e.e.

In this research, different conformers and its rotamers are generated with a tool called CREST introduced by P.Pracht et al. in 2020. It creates a set, which is called a conformer/rotamer ensemble (CRE), with conformers and their rotamers within a certain energy window around the global covalent potential energy minimum.

The rotamers must also be taken into account to get an accurate Gibbs free energy of binding [28]. Conformers belong to a set of stereoisomers with each an distinct energy minimum. Rotamers arise when there is a rotation around a restricted bond. They have identical energies, but their atomic coordinates differ as a result of the interchange of nuclei [29, 30].

The conformers are generated at the GFN2-xTB level within the iMTD-GC workflow [30]. GFN2-xTB is a semi-empirical tight-binding model. In this model, the short-range dispersion interactions are included, which makes it less empirical and more accurate compared to other semi-empirical models [28]. Several studies show that GFNn-xTB methods are one of the best performing semi-empirical methods for conformational energies [31, 32]. However, compared to DFT level, it gives less accurate energies. The reason that GFN2-xTB is still chosen for CREST is that it generates reasonable geometries for a vast amount of structures at short computation times [33–35].

The workflow makes use of iterative meta-dynamics (MTDs) and genetic structure crossing algorithms (GC) [28] and is depicted in Figure 2.2a. The first three steps of the workflow include MTD simulations, MD sampling and GC. These steps generate structures for the intermediate CRE. The final CRE is obtained after distinction between identical isomers, conformers and rotamers and thus does not include duplicates. The distinction is made by comparison of three parameters to their threshold values. The three parameters are: the root-mean-square deviation (RMSD), the rotational constants (B_e) and the electronic energy (E) [29, 30]. Only when the values for the three parameters are equal for the isomers, then they are categorised as duplicates [30]. The distinction is outlined in Figure 2.2b.

Since in this research CREST calculations are performed on transition state structures, the constrainment application is used. In this case, the Ir, N, C and H atoms of the transition state structure which partake in the reaction, will be constrained. Possible conformers can thus be generated while the reaction site remains the same [36].

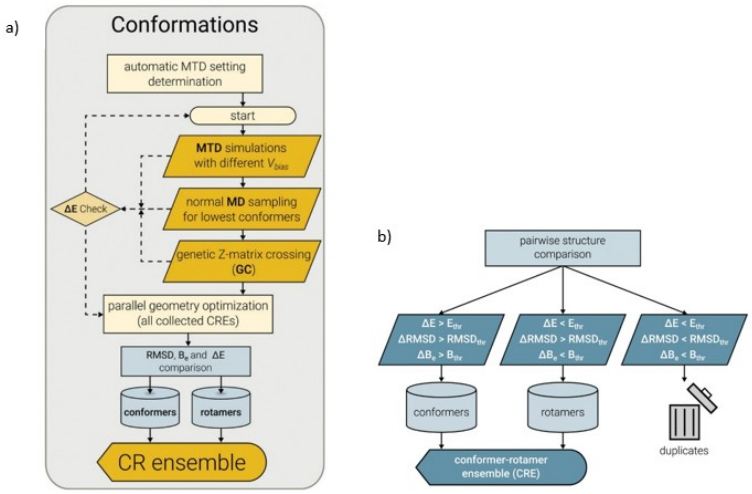

Figure 2.2: a) Automatized quantum chemical sampling procedure for conformers. b) schematic representation of the sorting criteria to distinguish between identical sturctures, conformers and rotamers. E_{thr}, $RMSD_{thr}$ and B_{thr} are the predefined thresholds [30].

2.3. Root-mean-square deviation (RMSD)

RMSD is one of the most popular methods to quantify the difference in geometry between two structures [37]. RMSD is used in this research project to compare the geometry of the transition states generated by DFT with the best conformers of the transition states generated by GFN2-xTB with CREST. Two conformations of the same transition state will thus be compared.

The RMSD is calculated according to Equation 2.2:

$$RMSD(V,W) = \sqrt{\frac{1}{N} \cdot \sum_{i=1}^{N} ((V_{ix} - W_{ix})^2 + (V_{iy} - W_{iy})^2 + (V_{iz} - W_{iz})^2)} \tag{2.2}$$

where V and W indicate the two molecules which are compared and N stands for the number of atoms which must be the same in both structures. The first step in computing the RMSD is to bring the two structures

as close as possible to each other. This is done by proper rotation and translation of the two superimposed molecules. The structures are thus considered to be rigid [38]. In this research, the RMSD is calculated with a utility provided by a program called Chemcraft [39].

3

Results and discussions

In this chapter the results of the two proposed mechanisms are presented. The inner sphere C-migration mechanism will be discussed first in section 3.1. This section is divided in three subsections. The proposed mechanism is described in subsection 3.1.1 whereafter the results of the DFT calculations are given in subsection 3.1.2. There are multiple coordination sites at which the substrate can bind to the complex. Each option is analysed with the use of Gibbs free energy diagrams to see which option is the most thermodynamically favourable and thus more likely to occur. Moreover, in subsection 3.1.3 an analysis is given of the possible conformers of the transition states (TS) of three paths of the inner sphere C-migration mechanism. The outer sphere mechanism will be discussed in section 3.2. This section is also divided in multiple subsections: a description of the proposed mechanism and the results of the DFT calculations are given in subsection 3.2.1 and subsection 3.2.2 respectively.

3.1. Inner sphere C-migration mechanism

3.1.1. Proposed mechanism

Figure 3.1a depicts the general structure of the iridium catalyst with the bidentate JosiPhos ligand. It forms an octahedral molecular geometry with six symmetrically arranged coordination sites. The bidentate ligand is bound to the metal center at two equatorial coordination sites with the phosphorous atoms. The other coordination sites are indicated with the numbers 1 to 4, whereof the numbers one and two correspond to the axial positions and three and four to the equatorial positions.

The general reaction which is investigated in this research is depicted in Figure 3.1b. The substrate 2-Methyl-1-pyrroline together with hydrogen gas is converted into two enantiomers: (S)-2-Methyl-1-pyrrolidine and (R)-2-Methyl-1-pyrrolidine. Depending at which coordination site the substrate binds to the complex, the formation of one of the enantiomers is favoured over the other one.

In this research multiple paths for the same mechanism (inner sphere C-migration) are investigated. The various options arise because the substrate (2-Methyl-1-pyrroline) can bind to the complex at four different coordination sites. The proposed mechanism is based on a mechanism which is presented in literature. B. Tutkowski et al. investigated four possible reaction mechanisms for AH of an acyclic imine. One of those mechanisms was the inner sphere C-migration path [6]. Based on this mechanism, a similar mechanism is proposed for the AH of the cyclic 2-Methyl-1-pyrroline. A general indication, without specifying where the substrate binds, is given in Figure 3.1c. However, this mechanism is not given in its complete form; the last few steps of the mechanism are left out because no DFT calculations are performed on that part. The reason for that is because they do not determine the enantioselectivity of the product.

The mechanisms starts off with a substitution reaction where complex **1** is converted into complex **2**. Complex **1** has three coordinated hydrides and one η^2-coordinated dihydrogen molecule. This is the assumed starting complex under high hydrogen pressure since the oxidation state of the iridium is +3. For the substitution reaction, the 2-Methyl-1-pyrroline substrate enters the coordination sphere which results in the replacement of the H_2 molecule with the substrate. In all cases, the substrate binds to the metal center with a lone electron pair on the N-atom. Structures which involve η^2-coordination of the C=N bond of the substrate with the iridium center are also investigated in this research. However, after geometry optimization of these complexes, they converged into structures where the substrate binds with the lone electron pair on

the N-atom to the center. For almost all investigated paths, complex **3** remains in the same conformation as complex **2** and is indicated as $\mathbf{3_a}$. However, there are two paths ($3R_2$ and $4R_3$) where the complex forms a π-coordinated complex: $\mathbf{3_b}$. Then, the C=N bond of the substrate interacts with the iridium center. The $\mathbf{3_b}$ complex was found because it has a local minimum on the PES.

The next step in the reaction mechanism is the hydrogenation of the C-atom which was part of the C=N bond of the substrate (C*). One of the hydrides forms a bond with the C*-atom which leaves an empty coordination site on the iridium center. This hydride transfer is the stereoselective step of the whole reaction mechanism. For the formation of complex **4**, an energy barrier must be overcome. The height of the barrier differs for the various investigated paths and is defined as the ΔG between complex **3** and the transition state $\mathbf{TS_{3->4}}$. The following step is the association of a dihydrogen molecule to the complex. This reaction step has a large reaction speed due to the high hydrogen gas pressure. The formed complex is indicated with number **5**. Hydrogenation of the N-atom of the substrate is the next step in the proposed reaction mechanism. However, since no calculations are performed on this part, the geometries of the structures are not given. The final step is a substrate dissociation and an H_2 association to the complex. The resulting product is a racemic mixture of the 2-Methyl-1-pyrroline enantiomers.

Different paths will result in different values for the enantiomeric excess. To specify which path is the most thermodynamically favourable and which enantiomer is preferred in the reaction, DFT calculations are performed. The hydride transfer to the C* atom of the substrate is the stereoselective step in the whole reaction mechanism. Therefore, the pathway with the lowest Gibbs free energy change to $\mathbf{TS_{3->4}}$ should be the overall favoured pathway. An overview of these barriers of all the investigated paths are presented in Table 3.1. The findings of the DFT calculations are given in subsection 3.1.2.

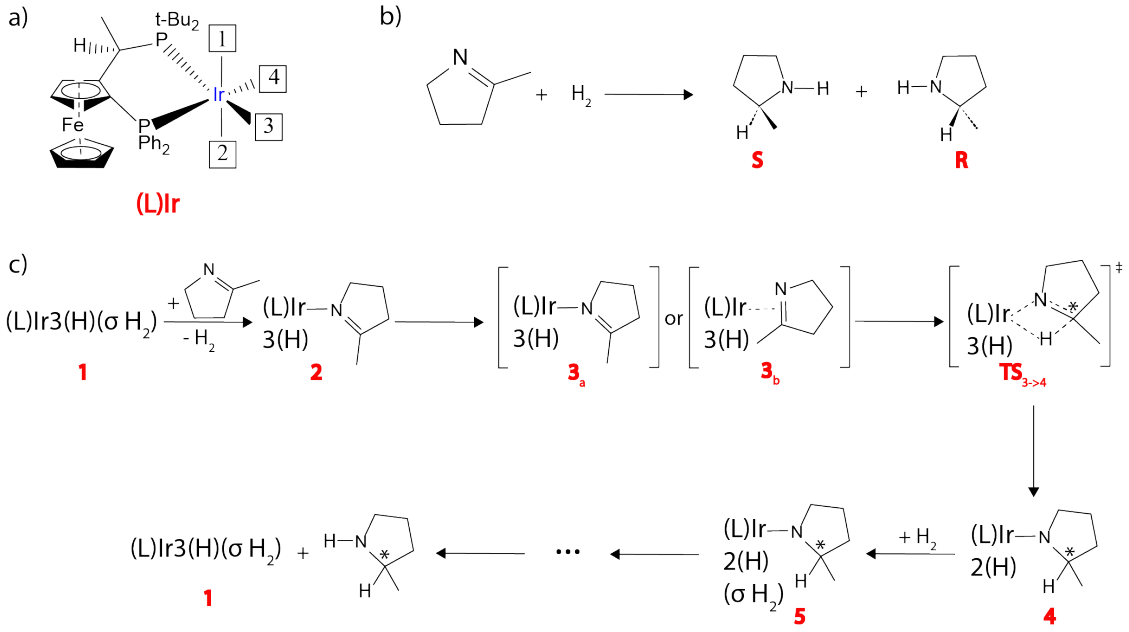

Figure 3.1: a) Iridium complex with equatorial coordinated JosiPhos ligand. b) General reaction for the formation of the S and R enantiomer. c) Mechanistic proposal for the inner sphere C-migration path.

3.1.2. Results DFT calculations

As was mentioned in subsection 3.1.1, the substrate can bind to the metal center at four different coordination sites (1 to 4). For each option, the Gibbs free energy diagrams of the various paths are presented in Figure 3.3. The paths are indicated with different colors and it is specified which enantiomer (S or R) is formed with a certain path. The visualization of the structures of the paths is given in separate figures to keep the diagrams clear. These figures are presented in Appendix B.

In the Gibbs free energy diagrams in Figure 3.3, the Gibbs free energy (G) of the complexes **2** to **5** are relative to the G of the separated catalyst and the substrate, indicated with complex **1**. The Gibbs free energy is calculated according to Equation 3.1:

$$G = H - T \cdot S \tag{3.1}$$

where H represents the enthalpy, T the temperature and S the entropy. In this research, all DFT calculations are performed at a temperature of 298.15 Kelvin. Thus the difference in Gibbs free energy of the complexes can be caused by a different value for the enthalpy or entropy. The values of the electronic energy (E), zero-point energy (ZPE), enthalpy (H) and the Gibbs free energy (G) of the structures of all investigated paths are given in Appendix A.

Before going into the details of the Gibbs free energy diagrams in Figure 3.3, the energy barrier which determines the favourability of the path is discussed first. Multiple articles about AH of imines suggest that the favourability of a certain reaction path is determined by the stereo-determining step. The free energy barrier to the corresponding transition state is then considered [6, 40]. In this research, this corresponds to the $\Delta G_{3_{a,\,3S}\text{->}TS_{3\text{->}4}}$ for all investigated paths. The Gibbs free energy of complex $3_{a,\,3S}$ is taken as a reference. For each path, the values of the **$TS_{3\text{->}4}$** relative to complex $3_{a,\,3S}$ are compared to each other to determine which path is the most favourable.

The reason why complex $3_{a,\,3S}$ is taken as a reference is because of kinetics. Figure 3.3 shows the G of complexes **3** of each investigated path relative to the G of complex **1**. It can be seen that complex $3_{a,\,3S}$ in Figure 3.3c has the lowest value: -50 kJ/mol. Thus for each path, $3_{a,\,3S}$ will be formed first. It is assumed that the constitutional isomers of complex **3** are in equilibrium with each other. For paths other than 3S, the complex $3_{a,\,3S}$ must first be converted into the complex **3** of that certain path. Thus, an extra energy barrier must be overcome. To conclude, the lower the value of $\Delta G_{3_{a,\,3S}\text{->}TS_{3\text{->}4}}$, the more favourable the the path is since the barrier for the stereo-determining step is lower. These values are depicted in Table 3.1. Now, the different paths per option will be discussed one by one.

Path	1S	1R	2S	3S	$3R_1$	$3R_2$	4S	$4R_1$	$4R_2$	$4R_3$
$\Delta G_{3_{a,\,3S}\text{->}TS_{3\text{->}4}}$ (kJ/mol)	151	161	180	105	124	106	112	190	121	132

Table 3.1: An overview of the $\Delta G_{3_{a,\,3S}\text{->}TS_{3\text{->}4}}$ of all the investigated paths.

Coordination site 1

The Gibbs free energy diagrams of the paths where the substrate binds to coordination site 1 will be described first and are depicted in Figure 3.3a. The corresponding structures for the 1S and 1R path are given in Figure B.1 in Appendix B. $\Delta G_{3_{a,\,3S}\text{->}TS_{3\text{->}4}}$ is 161 kJ/mol for the formation of the R enantiomer (path 1R) and 151 kJ/mol for the formation of the S enantiomer (path 1S). These values indicate that on this position the formation of the S enantiomer is preferred. The Gibbs free energy change is relatively large compared to other $\Delta G_{3_{a,\,3S}\text{->}TS_{3\text{->}4}}$ values presented in Table 3.1. This indicates that the energy barrier is high and that the 1S and 1R path are not the most favourable.

The reason why the G of **$TS_{3\text{->}4,\,1S}$** (101 kJ/mol) is lower than the G of **$TS_{3\text{->}4,\,1R}$** (111 kJ/mol) can be explained with the three-dimensional transition state structures. These structures are depicted in Figure 3.2 and in each TS structure three atomic distances are shown.

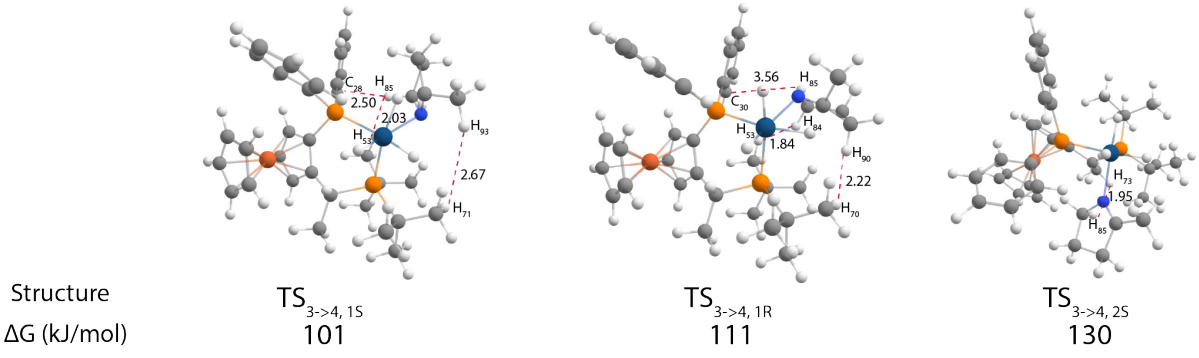

Figure 3.2: Three dimensional transition state structures of the complexes for the 1S, 1R and 2S.

The atomic distance between H_{85} and C_{28} in the $TS_{3\text{->}4,\,1S}$ structure is 2.50 angstrom while the atomic distance in the $TS_{3\text{->}4,\,1R}$ structure is 3.56 angstrom between H_{85} and C_{30}. These values indicate that the sub-

strate is more closely oriented to the phenyl (Ph) group in $TS_{3->4,\,1S}$. Moreover, the atomic distances between H_{53} and H_{85} and between H_{70} and H_{90} in $TS_{3->4,\,1R}$ are 1.84 and 2.22 angstrom respectively. The distance between H_{71} and H_{93} in $TS_{3->4,\,1S}$ is 2.67 angstrom. These values represent the distance between the substrate and the tert-Butyl (t-Bu) groups and indicate that the substrate in the $TS_{3->4,\,1R}$ is oriented more closely to the t-Bu groups compared to $TS_{3->4,\,1S}$; the substrate experiences more steric repulsion by the t-Bu groups. This could be a possible explanation why the transition state of the 1R path has a higher Gibbs free energy.

Furthermore, there are two more remarkable findings. The Gibbs free energy for the first step in the reaction stays the same for paths 1S and 1R. This indicates that the substitution reaction is neither endothermic nor exothermic. When looking at the other Gibbs free energy diagrams of the other options, the ΔG does go down for the first step. A possible reason why this does not occur for the paths at position 1 remains unclear. It cannot be explained by the presence or absence of steric hindrance by the JosiPhos ligand, because the distance between the Ph/t-Bu groups and the substrate is relatively small.

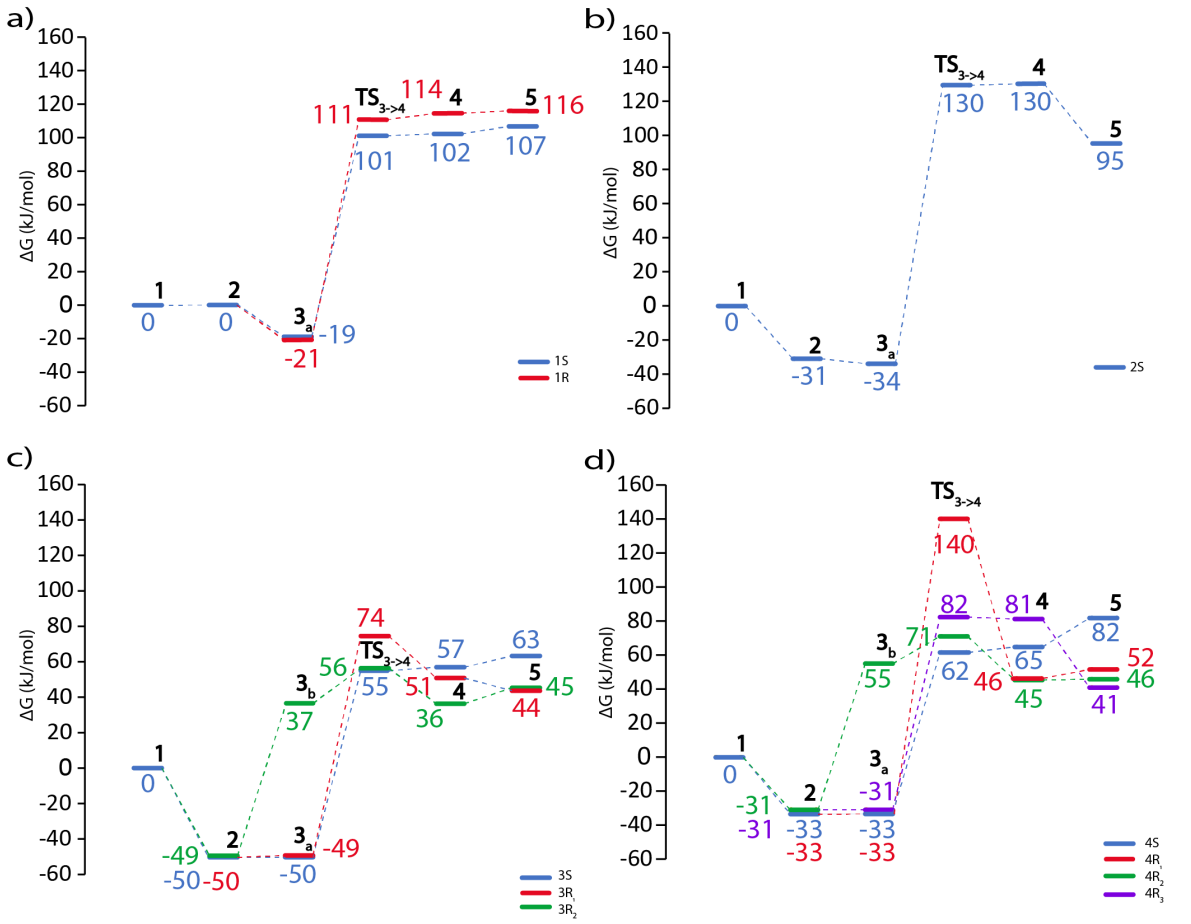

Figure 3.3: This figure shows the Gibbs free energy diagrams of the four coordination options for the substrate on the catalyst complex. The Gibbs free energy of each state of the formation of the S enantiomer is given. a) The substrate is bound to the complex at position 1. The formation of the S and R enantiomer is given in blue and red respectively. b) The substrate is bound to the complex at position 2. c) The substrate is bound to the complex at position 3. The formation of the S enantiomer is given in blue. The R_1 and R_2 enantiomers are given in red and green. The difference is the spacial placement of the substrate; for the formation of R_1, the methyl group of the substrate is faced upwards and for the formation of R_1, the methyl group is faced downwards. d) The substrate is bound to the complex at position 4. This diagram shows four options: only one of them generates a S enantiomer (blue) and the other ones the R enantiomer (red, green, purple). The difference between them is the spacial orientation of the substrate bounded to the complex.

The second remarkable thing is that for both paths, complex **4** and **5** are higher in Gibbs free energy than the transition state. This is an unusual event, because the transition state should be a maximum in energy. However, it should be noted that the given values are Gibbs free energies. The G is calculated according to Equation 3.1. According to the enthalpy values given in Appendix B, the enthalpy of complex **4** is approximately 4 kJ/mol higher than the enthalpy of **$TS_{3->4}$** for both paths. The $\Delta G_{TS_{3->4}->4}$ is 3 kJ/mol for path 1R and 1 kJ/mol for path 1S. This free energy difference can thus be explained by the enthalpy difference and not the

entropy difference.

Coordination site 2

In Figure 3.3b the Gibbs free energy diagram is given of the path where the substrate binds to coordination site 2. The corresponding structures for the 2S path are given in Figure B.1 in Appendix B. Only the path for the formation of the S enantiomer is given (path 2S). The $\Delta G_{3_{a,\,3S}\text{->}TS_{3\text{->}4}}$ for this path is relatively large, namely 180 kJ/mol. This is an endergonic step. Calculations on the path for the formation of the R enantiomer did not give suitable data because the transition state would not converge. However, it can be concluded that position 2 is not a thermodynamically favourable coordination site for the substrate because the energy barrier of 180 kJ/mol is the second largest barrier of all investigated paths.

To understand the large $\Delta G_{3_{a,\,3S}\text{->}TS_{3\text{->}4}}$, a three-dimensional structure of **$TS_{3\text{->}4,\,2S}$** is presented in Figure 3.2. The atomic distance between H_{73} and H_{85} is 1.95 angstrom. This indicates that the substrate is close to t-Bu groups of the JosiPhos ligand and thus experiences steric hindrance and repulsion. Moreover, the phenyl group is pointed towards the substrate instead of oriented parallel to the substrate. The hindrance of the Ph group and the t-Bu groups has as a consequence that the catalytic pocket of coordination site 2 is relatively small. This could be the reason why the $\Delta G_{3\text{->}TS_{3\text{->}4}}$ for the 2S path is relatively high.

Furthermore, the large free energy drop from complex **4** to complex **5** is because of the large difference in enthalpy: -3082 kJ/mol. However, there is also a large entropy difference of +3037 kJ/mol. This results in a Gibbs free energy change of -45 kJ/mol.

Coordination site 3

In Figure 3.3c the Gibbs free energy diagrams are given of the paths where the substrate binds to coordination site 3. The corresponding structures for the 3S, $3R_1$ and $3R_2$ paths are given in Figure B.2 in Appendix B. The Gibbs free energies of the transition states of each path are relatively low compared to transition states of the other options. The $\Delta G_{3_{a,\,3S}\text{->}TS_{3\text{->}4}}$ for the paths 3S, $3R_1$ and $3R_2$ are 105 kJ/mol, 124 kJ/mol and 106 kJ/mol respectively. Paths 3S and $3R_2$ have the lowest values for the $\Delta G_{3_{a,\,3S}\text{->}TS_{3\text{->}4}}$ and thus can be considered the two most favourable paths. The Gibbs free energy difference between these two paths is minimal: 1 kJ/mol. Based on this information, there is no substantial preference for the formation of one enantiomer over the other.

The main difference between the $3R_2$ path and the 3S path is the Gibbs free energy of complex **3**. This large difference in energy can be explained by looking at the three-dimensional structures of **3_a** and **3_b**, which are depicted in Figure 3.4. The substrate in complex $3_{a,\,3S}$ is coordinated to the iridium center with a lone electron pair on the N-atom. This is different for the substrate in the $3_{b,3R_2}$. As can be seen in the figure, the substrate has a η^2-coordination of the C=N bond with the center. This structure has a similar geometry as the transition state, because the TS is also a π-coordinated complex. The different orientation of the substrate in complex $3_{a,\,3S}$ and $3_{b,3R_2}$ is the reason for the large Gibbs free energy difference, -50 kJ/mol for complex $3_{a,\,3S}$ and 37 kJ/mol for complex $3_{b,3R_2}$.

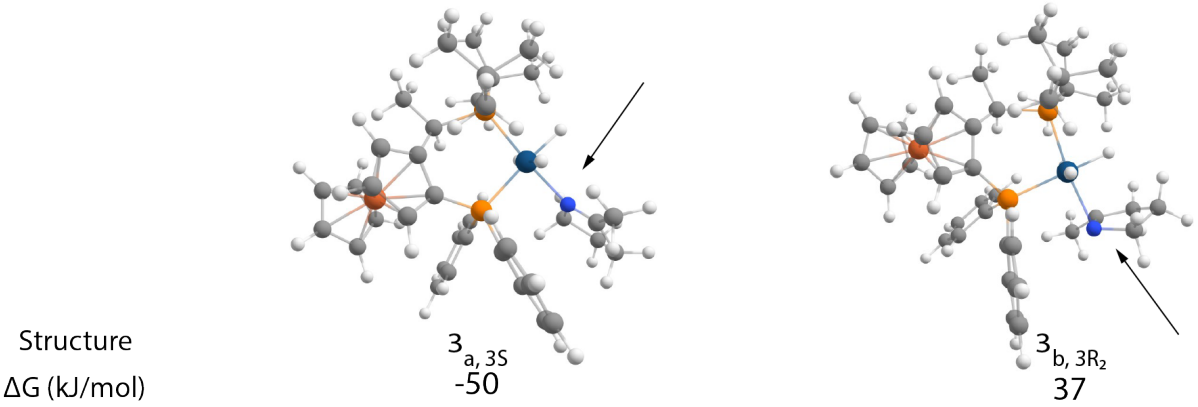

Figure 3.4: Three dimensional structures of the complexes 3_a and 3_b for the 3S and $3R_2$ path.

The $\Delta G_{3_{a,\,3S}\text{->}TS_{3\text{->}4}}$ for the $3R_1$ path is 124 kJ/mol which is higher than the other two paths. This path is therefore the least favourable of the three paths where the substrate binds on coordination site 3.

Furthermore, a comment can be made about Figure 3.3c. The Gibbs free energy of complex **4** is higher than that of **$TS_{3->4}$** for the 3S path; the difference is +2 kJ/mol. This reaction step is thus endergonic, which indicates that a less stable structure is formed. This phenomena is also seen in Figure 3.3a. Again, this increase in Gibbs free energy is due to the increase in enthalpy, since the enthalpy difference between **$TS_{3->4}$** and complex **4** of path 3S is approximately 3 kJ/mol. The entropy difference is thus very little. When looking at the same reaction step for the other paths, the Gibbs free energy goes down as expected.

Coordination site 4

In Figure 3.3d the Gibbs free energy diagrams are given of the paths where the substrate binds to coordination site 4. The corresponding structures for the 4S, $4R_1$, $4R_2$ and $4R_3$ paths are given in Figure B.3 in Appendix B. The $\Delta G_{3_{a,\,3S}->TS_{3->4}}$ for the four paths are given in Table 3.1. These values are all higher than the values for path 3S and $3R_2$, thus coordination site 4 is considered not to be the best coordination site for the substrate to bind to the catalyst complex.

In Figure 3.3 it is remarkable to see that complex **3_b** of path $4R_2$ is much higher in Gibbs free energy than complex **3_a** of the other paths. The G of complex **3_b** of path $4R_2$ ($3_{b,\,4R_2}$) is 55 kJ/mol and the G of complex **3_a** of the 4S path ($3_{a,\,4S}$) is -33 kJ/mol. This difference can be explained by the orientation of the substrate at the coordination site. Three-dimensional structures of complexes $3_{b,\,4R_2}$ and $3_{a,\,4S}$ are depicted in Figure 3.5. This case is similar to the 3S and $3R_2$ paths. The substrate in the 4S path is coordinated with a lone electron pair on the N-atom, while the substrate has an η^2-coordination of the C=N bond with the center in the $4R_2$ path. The difference in coordination explains the large energy difference.

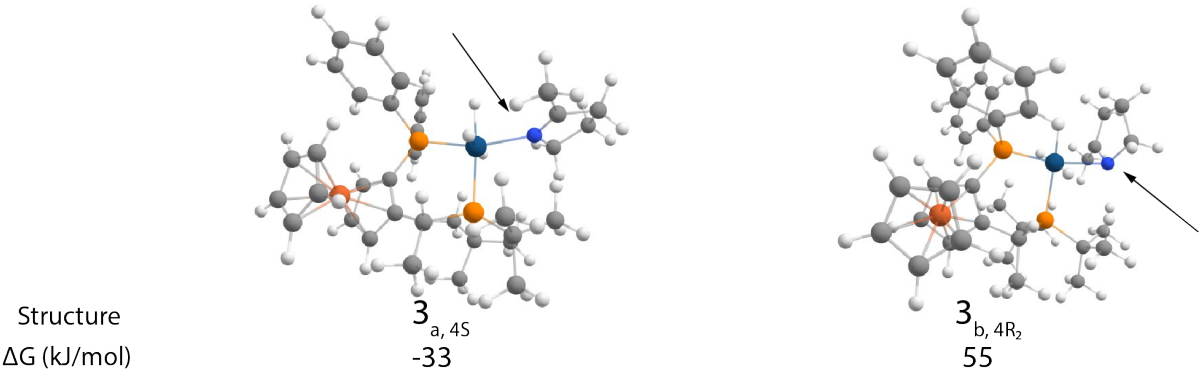

Figure 3.5: Three dimensional structures of complexes 3_a and 3_b for the 4S and $4R_3$ path.

Furthermore, the $4R_1$ path stands out because it has the highest $\Delta G_{3_{a,\,3S}->TS_{3->4}}$ value, namely 190 kJ/mol. This is because the transition state has a very high Gibbs free energy: 140 kJ/mol. It can be said that this is the most unfavourable path. A possible explanation for the high energy of the **$TS_{3->4}$** of path $4R_1$ ($TS_{3->4,\,4R_1}$) is given based on the three-dimensional structures of the transition states of the four paths. These structures are depicted in Figure 3.6. For clarity, $TS_{3->4,\,4S}$ and $TS_{3->4,\,4R_1}$ are compared to each other since these two structures have the most extreme values of the four paths. In the $TS_{3->4,\,4R_1}$, the methyl group of the substrate is pointed towards the Ph groups and the ring of carbon atoms is oriented towards the t-Bu groups. The orientation of the substrate in $TS_{3->4,\,4S}$ is different than in $TS_{3->4,\,4R_1}$; the methyl group of the substrate is pointing in between the Ph and t-Bu groups and the ring of carbon atoms is less closely oriented to the t-Bu groups. Even though the closest distance between the substrate and the Ph group is smaller (2.21 angstrom) in $TS_{3->4,\,4S}$ compared to the $TS_{3->4,\,4R_1}$ (2.53 angstrom), the substrate experiences more steric repulsion in the $TS_{3->4,\,4R_1}$. This is because in path $4R_1$ the hydrogen atoms connected to the carbon atoms in the ring are relatively close to the t-Bu groups. The distance between H_{71} and H_{84} is only 1.97 angstrom. This is a smaller distance than that of H_{62} and H_{85} in $TS_{3->4,\,4S}$, which is 2.21 angstrom. This could be the reason why the Gibbs free energy of the $TS_{3->4,\,4R_1}$ is higher than of the $TS_{3->4,\,4S}$.

Moreover, the TS of paths $4R_2$ ($TS_{3->4,\,4R_2}$) and $4R_3$ ($TS_{3->4,\,4R_3}$) are higher in Gibbs free energy than the $TS_{3->4,\,4S}$ structure. The substrate is located more closely to the t-Bu groups in the $4R_2$ and $4R_3$ paths compared to the 4S path. The distance between H_{62} and H_{93} in the $TS_{3->4,\,4R_2}$ is 1.79 angstrom and the distance between H_{73} and H_{84} in the $TS_{3->4,\,4R_3}$ is 2.00 angstrom. These distances are smaller than the distance of 2.21 angstrom in $TS_{3->4,\,4S}$, which indicates that the substrate is closer to the t-Bu groups in the $TS_{3->4,\,4R_2}$ and

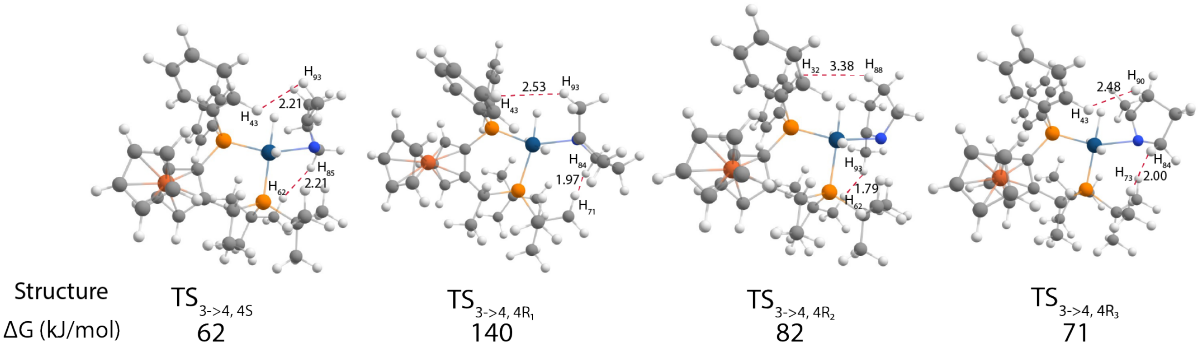

Figure 3.6: Three dimensional transition state structures of the complexes for the 4S, $4R_1$, $4R_2$ and $4R_3$ path.

$TS_{3->4,\ 4R_3}$ structures. This could be the reason why the Gibbs free energy of the transition states of paths $4R_2$ and $4R_3$ are higher than of path 4S.

Lastly, in Figure 3.3d it can be seen that complex **4** and **5** of path 4S are higher in Gibbs free energy than **$TS_{3->4}$**. The $\Delta G_{TS_{3->4}->4,\ 4S}$ is +3 kJ/mol. The enthalpy difference between $TS_{3->4,\ 4S}$ and complex 4_{4S} is also 3 kJ/mol. The entropy difference is thus very little and the difference in free energy therefore has an enthalpic origin. The enthalpy difference between complex **4** and **5** of path 4S is large, namely 3028 kJ/mol. However, the entropy difference is also very large which results in an overall Gibbs free energy increase of 17 kJ/mol. The enthalpy values of the complexes can be found in Appendix A.

3.1.3. Conformers of transition states

In this subsection, the importance of ensemble representation is discussed. Ensemble representations are considered in this research to investigate their influence on the enantioselectivity. Therefore, a conformer search is done on the transition states of paths 3S, $3R_1$ and $3R_2$ with a tool called CREST. Multiple conformers were found of which one had the lowest energy and is considered to be the best conformer. First, a comparison is made between the best conformer found by GFN2-xTB calculations with CREST and the transition state found by DFT calculations. For each path, the electronic energy difference between these structures is given in Table 3.2 and their geometries are depicted in Figure 3.7. ΔE_{TS} is computed by subtracting the electronic energy of the TS generated by DFT from that of the TS generated with CREST. Then, the Gibbs free energies of the structures of the different paths are compared to each other. The Gibbs free energy is derived by correcting the electronic energy with the zero-point energy and an entropy term [12]. ΔG_{TS} is computed by subtracting the Gibbs free energy of the TS generated by DFT from that of the TS generated with CREST. The focus lies on the 3S and $3R_2$ paths since they nearly have the same energy barrier for the stereo-determining step (105 kJ/mol and 106 kJ/mol) when only considering the structures generated by DFT. This indicated that there was no substantial preference for the formation of one enantiomer over the other. Therefore, conformers are compared in Gibbs free energy to see if there arises a preference for the formation of one enantiomer.

Path 3S

Now, the transition state structures of the 3S path will be discussed. In total seven conformers were found. The difference in energy between the best and the worst conformer is 19 kJ/mol. Their geometries differ significantly from each other. $TS_{3S,DFT}$ has a lower energy than the best found conformer ($TS_{3S,CREST}$). The electronic energy difference is +7 kJ/mol (see Table 3.2) which indicates that the found conformer is less stable than the structure generated by DFT. The difference in geometry is also clearly visible in Figure 3.7a. The phenyl groups, the ferrocene and the tert-Butyl groups are oriented differently. The orientation of the substrate remained the same. The RMSD between the two structures is 1.730 angstrom.

Path	ΔE_{TS} (kJ/mol)	ΔG_{TS} (kJ/mol)	RMSD
3S	7	5	1.730
$3R_1$	3	4	2.993
$3R_2$	-9	-9	1.404

Table 3.2: The energy difference, Gibbs free difference and the RMSD between the transition state structures generated by DFT and GFN2-xTB with CREST for the paths 3S, $3R_1$ and $3R_2$. $\Delta E_{TS}=E_{TS,CREST}-E_{TS,DFT}$ and $\Delta G_{TS}=G_{TS,CREST}-G_{TS,DFT}$.

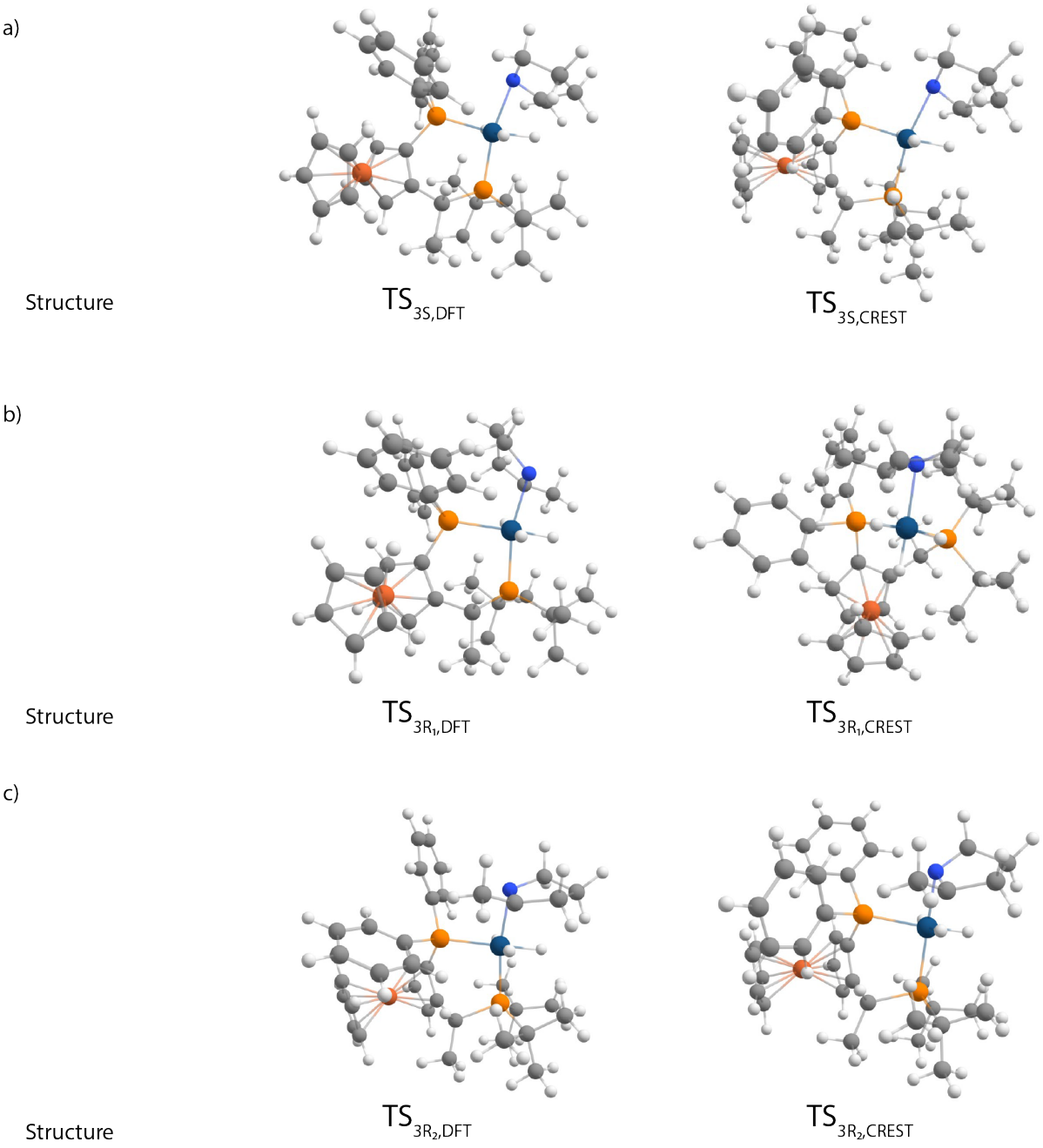

Figure 3.7: The transition states structures generated by DFT and GFN2-xTB with CREST of path 3S, $3R_1$ and $3R_2$.

Path $3R_1$

Conformers of the transition state of the $3R_1$ path were also found. In total there are five conformers found with CREST. The energy difference between these five structures lies in a range of 19 kJ/mol. Only one of those five structures differs significantly from the rest and has a higher energy. The energy and geometry of the remaining structures were nearly the same. The best conformer $TS_{3R_1,CREST}$ has a slightly higher energy than the structure generated with DFT ($TS_{3R_1,DFT}$). The electronic energy difference is +3 kJ/mol and is depicted in Table 3.2. The found conformer is again less stable than the structure generated by DFT. The corresponding geometries are depicted in Figure 3.7b. The difference in energy can be explained by the change in geometry. In the $TS_{3R_1,DFT}$ structure, the substrate is bound to the iridium center at position 3, while it is bound at position 1 in the $TS_{3R_1,CREST}$ structure. Thus, CREST can vary the coordination site of ligands to the metal center when finding possible conformers. This is also the reason why the RMSD is relatively large compared

to the transition states of the other paths. The RMSD is 2.993 angstrom and is given in Table 3.2. Furthermore, the orientation of the Ph groups and the ferrocene is different. The ferrocene is pointing more towards the substrate in the $TS_{3R_1,CREST}$ structure and the Ph groups have rotated.

Path $3R_2$
Now, the transition state structures of the $3R_2$ path will be discussed. In total 272 conformers of this TS were found. The difference in energy between the best and the worst conformer is 25 kJ/mol. Most conformers differ only slightly in their geometry. However, some conformers do have a significant different geometry. For example when the phenyl groups rotate with approximately 90 degrees. The best conformer ($TS_{3R_2,CREST}$) has a lower electronic energy than the $TS_{3R_2,DFT}$ structure. The energy difference is -9 kJ/mol and is given in Table 3.2. These values indicate that the best conformer of this transition state is more stable than the structure generated by DFT. The geometries are depicted in Figure 3.7c. It can be seen that the phenyl groups have a different orientation. In the $TS_{3R_2,CREST}$ structure, the phenyl groups are rotated approximately 90 degrees compared to the $TS_{3R_2,DFT}$ structure. The rest of the structure differs only slightly. The RMSD between the two structures is 1.404 angstrom. Compared to the other paths, this is the lowest RMSD value. Thus the best conformer is the most similar to the DFT generated TS structure based on geometry for path $3R_2$.

For path 3S and $3R_1$, the found conformers were less stable than the transition state structures generated by DFT. Only the best conformer of the transition state of path $3R_2$ is more stable than the DFT structure because it has a lower energy. However, the Gibbs free energy of the structures must be considered to know if the $\Delta G_{3_{a,\,3S}\text{->}TS_{3\text{->}4}}$ becomes lower. For paths 3S, $3R_1$ and $3R_2$, the difference in Gibbs free energy of the transition states generated by DFT and GFN2-xTB with CREST is depicted in Table 3.2. For paths 3S and $3R_1$, the structures generated by GFN2-xTB have a higher Gibbs free energy than the structures generated by DFT. The ΔG_{TS} is +5 kJ/mol and +4 kJ/mol respectively. The Gibbs free energy of TS_{CREST} is lower than that of TS_{DFT} for path $3R_2$ which results in a ΔG_{TS} of -9 kJ/mol. The $\Delta G_{3_{a,\,3S}\text{->}TS_{3\text{->}4},\,3R_2}$ thus becomes 97 kJ/mol instead of 106 kJ/mol while the $\Delta G_{3_{a,\,3S}\text{->}TS_{3\text{->}4}}$ for path 3S remains 105 kJ/mol. When considering the best conformer for path $3R_2$, there arises a preference for the formation of the R enantiomer. However, it should be noted that the difference between the heights of the barriers remains small: 8 kJ/mol.

3.2. Outer sphere mechanism

3.2.1. Proposed mechanism

The initial guess for mechanism of the outer sphere path is based on the outer sphere mechanism for the AH of an acyclic imine described by B. Tutkowski et al. in 2017. The proposed mechanism for the AH of 2-Methyl-1-pyrroline is depicted in Figure 3.8a. The first step in the reaction is the hydrogenation of the N-atom of the substrate. This occurs in the outer sphere of the catalyst as the name of the mechanism suggests. A hydrogen atom coming from the dihydrogen molecule coordinated to the center is translated to the N-atom. The remaining hydrogen is then bound to the metal center as a hydride. The result is a negatively charged catalyst complex with in the outer sphere a positively charged substrate.

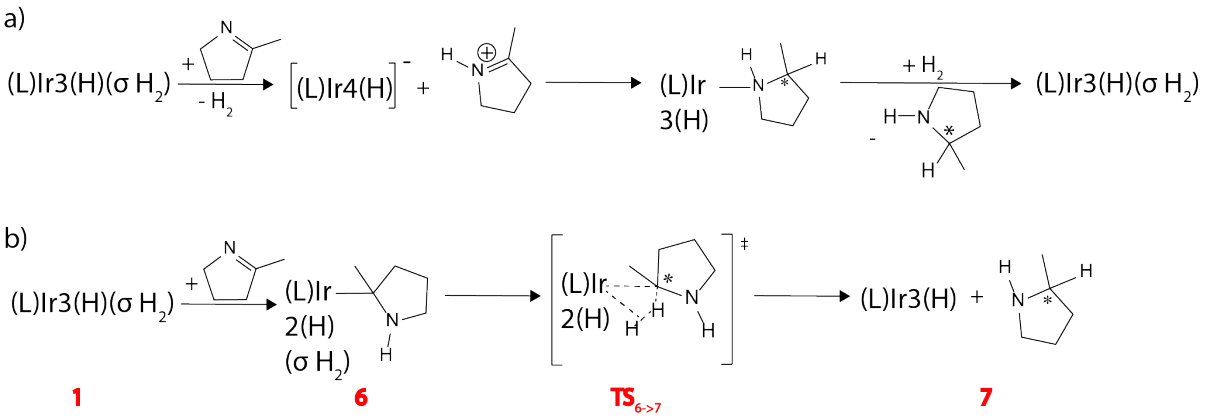

Figure 3.8: a) Proposed outer sphere mechanism based on literature. b) Reaction mechanism found when the substrate is coordinated to position 3 on the catalyst complex.

The next step in this reaction mechanism is the hydrogenation of the carbon atom which was part of the C=N bond in the substrate (C*). This step is the stereo-determining step. Depending on which of the four hydrides coordinated at the iridium center reacts with the C*, the S or R enantiomer is formed. The last step of the mechanism is the dissociation of the substrate and the association of the dihydrogen molecule which results in the same structure as the starting complex.

There are four coordination sites for the substrate (2-Methyl-1-pyrroline) to bind to the catalyst complex. These coordination sites are indicated with numbers 1 to 4 as is depicted in Figure 3.1a. Therefore, multiple reaction paths arise for the same reaction mechanism (the outer sphere mechanism). However, due to limited time to perform the DFT calculations, not all paths could be investigated. Only the reactions paths of when the substrate binds to coordination site 1,2 and 3 are partially explored. When performing an energy scan for the stereo-determining step to find the transition state for the option where the substrate binds on coordination site 1 or 2, convergence was not reached. There was too little time to redo the calculations. Therefore, only one path for when the substrate binds on coordination site 3 is presented in this report in subsection 3.2.2.

During research, an attempt is made to create the mechanism depicted in Figure 3.9a. However, the DFT calculations gave other geometries. Therefore, a second mechanism for the outer sphere mechanism is presented which is based on the outcome of DFT calculations performed in this project. The mechanism that was found is depicted in Figure 3.8b. In the first reaction step, one of the hydrides coordinated to the iridium center reacts with the N-atom of the substrate in the outer sphere. After the protonation of the N-atom, the substrate is coordinated to the iridium center with a lone electron pair on the C-atom. The resulting structure is referred to as complex **6**. The next step is the formation of the transition state: $\mathbf{TS_{6->7}}$. One of the hydrogen atoms from the σ-coordinated dihydrogen molecule reacts with the C* atom of the substrate. The formed product is the chiral amine in the outer sphere and a catalyst complex with three coordinated hydrides (**7**). One of those hydrides originates from the dihydrogen molecule.

A difference between the two mechanisms depicted in Figure 3.8 is the coordination of the substrate. In the first step of the mechanism which is based on literature, the protonated substrate stays in the outer sphere while in the mechanism found in this research, the protonated substrate is bound to the iridium center with the C-atom (complex **6**). A possible explanation for this difference could be the instability of the protonated substrate. The acidity constant (pK_a) has a direct relevance to the stability and activity of the substrate [41]. The higher the pK_a value of the unprotonated substrate, the less stable the protonated substrate is. Tutkowski et al. describe the outer sphere mechanism for the reaction of another imine substrate, namely N,1-diphenylethanimine. The pK_a value of this substrate is 3.79±0.50. This entails that the conjugated acid (protonated substrate) is relatively stable. The substrate which reacts in this research is 2-methyl-1-pyrroline. It has a pK_a value of 8.41±0.20. The conjugated acid (protonated substrate) is thus relatively unstable. This could be the reason why it binds to the catalyst complex instead of staying in the outer sphere.

3.2.2. Results DFT calculations

The Gibbs free energy diagram of the path where the substrate binds to coordination site 3 is depicted in Figure 3.9. The blue path which leads to the formation of S-2-Methyl-1-pyrrolidine is indicated as $3S_2$. The corresponding structures for the $3S_2$ path is given in Appendix D.

The favourability of a certain path is determined by the height of the energy barrier of the stereoselective step of the reaction mechanism. In this case, the stereo-determining step is the hydrogenation of the C* atom of the substrate. Thus the height of the barrier corresponds to the Gibbs free energy change from complex **6** to $\mathbf{TS_{6->7}}$. As can be seen in Figure 3.9, the $\Delta G_{6->TS_{6->7}}$ of path $3S_2$ is 42 kJ/mol. However, since the formation of complex **6** is an endergonic step in the reaction, the $\Delta G_{1->6}$ must also be considered. This increase in Gibbs free energy must also fist be overcome for the reaction to be able to proceed. The favourability of this path is therefore determined by $\Delta G_{1->TS_{6->7}}$. Little can be said about the favourability of this path since there are no other paths investigated for this reaction mechanism already. Furthermore, a reasonable comparison between this mechanism and the inner sphere C-migration mechanism can also not be fully made. However, for this certain $3S_2$ path something can be said about the favourability compared to the inner sphere C-migration mechanism. The height of the barrier for path $3S_2$ is 117 kJ/mol. When only considering DFT calculations, the lowest barrier in the inner sphere C-migration mechanism is 105 kJ/mol (of path 3S). The barrier for the $3S_2$ is only slightly higher.

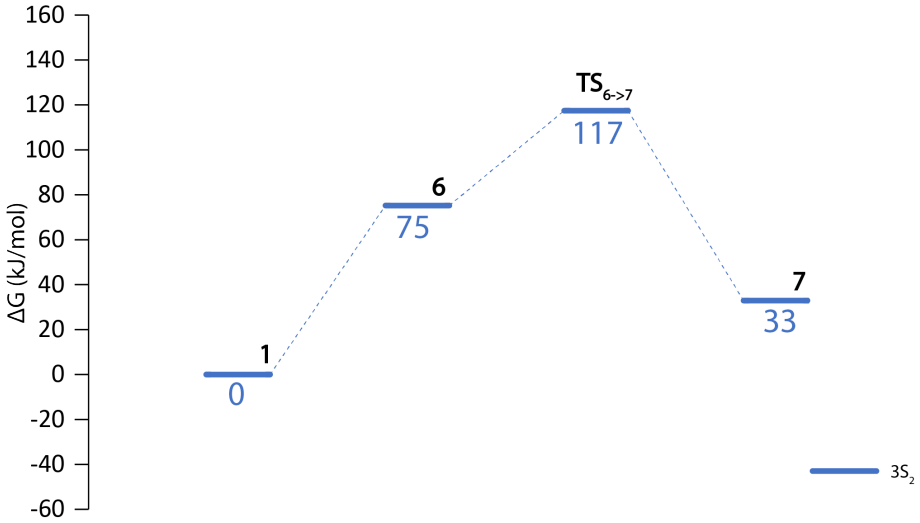

Figure 3.9: Gibbs free energy diagram of path $3S_2$ of the outer sphere mechanism which is proposed in Figure 3.8b.

4

Conclusions and Recommendations

4.1. Conclusions

The aim of this research was to get more insight in the reaction mechanism of the AH of 2-Methyl-1-pyrroline with an Ir-based catalyst with a JosiPhos ligand. DFT calculations were performed on two proposed reaction mechanisms: the inner sphere C-migration mechanism and the outer sphere mechanism. This research was focused more on the possible paths which arose for the inner sphere C-migration mechanism. Therefore, they will be discussed first. From the results of the DFT calculations, the following conclusions can be drawn:

- Coordination site 3 is thermodynamically the most favourable position for the substrate to bind to the catalyst. Path 3S and $3R_2$ are thermodynamically the most favourable since the Gibbs free energy barrier for the stereo-determining step ($\Delta G_{3_{a,\,3S}\text{->}TS_{3\text{->}4}}$) is the lowest compared to all investigated paths for the inner sphere C-migration mechanism. The $\Delta G_{3_{a,\,3S}\text{->}TS_{3\text{->}4}}$ for path 3S and $3R_2$ is 105 kJ/mol and 106 kJ/mol respectively. Therefore, this mechanism shows no preference for the formation of one enantiomer over the other when only considering structures generated by DFT.

- The remaining coordination sites (1,2 and 4) are thermodynamically less favourable for the substrate to bind to the catalyst. This could be due to the steric hindrance of the t-Bu and the Ph groups of the JosiPhos ligand.

- From Figure 3.3d it can be concluded that the barriers for different paths at the same coordination site can differ significantly. Path 4S has a $\Delta G_{3_{a,\,3S}\text{->}TS_{3\text{->}4}}$ of 112 kJ/mol while path $4R_1$ has a $\Delta G_{3_{a,\,3S}\text{->}TS_{3\text{->}4}}$ of 190 kJ/mol. The way the substrate is oriented at the coordination site and which hydride reacts with the substrate thus has an influence on the height of the barrier of the stereo-determining step. The enantioselectivity is also dependent on the orientation of the substrate, since different paths result in the formation of different enantiomers.

From the results of the conformer search it can be concluded that conformers found with CREST can have an influence on the height of the barrier of the stereo-determining step. For paths 3S and $3R_1$ the barriers remained the same because the best conformers were higher in G than the structures generated by DFT. However, for the $3R_2$ path, the barrier became smaller when considering the best conformer instead of the structure generated by DFT. The change in barrier height influences the enantioselectivity by making one path more favourable. When considering the best conformer of the TS of path $3R_2$, the inner sphere C-migration mechanism shows a preference for the formation of the R-enantiomer. The $\Delta G_{3_{a,\,3S}\text{->}TS_{3\text{->}4}}$ for path $3R_2$ is then namely lower than for path 3S.

DFT calculations for the outer sphere mechanism gave other geometries than was expected according to the mechanism which was proposed based on literature. Thus a second mechanism for the outer sphere mechanism was proposed. From the results of the DFT calculations, it can be concluded that path $3S_2$ is less thermodynamically favourable compared to the most favourable path of the inner sphere C-migration mechanism. However, there is not enough data to conclude whether the outer sphere mechanism is more likely to occur than the inner sphere C-migration mechanism.

4.2. Recommendations

Based on the results and conclusions of this research, the following recommendations are given for future research:

- Since the conformer search with CREST gave a more stable geometry of the TS of path $3R_2$, it is recommended to include conformer search of transition states in future research on reaction mechanisms as well. This might be useful because transition states with lower energies will then not be missed out on.
- Not many conclusions could be drawn about the outer sphere mechanism. Therefore it is recommended to further investigate this mechanism. Quantitative research is needed for all possible options for the coordination of the substrate to the catalyst. To verify which mechanism is the most likely one to occur, research is also needed on more mechanisms. For example the the inner sphere N-migration mechanism which is also reported by Tutkowski et al.
- For the energy scans which did not converge for the outer sphere mechanism, the input files can be adjusted. Extra coordinates can be added to ensure formation of certain bonds. During the scan, the C-H bond of the substrate is stretched. Coordinates can be added to ensure that the H-atom forms a bond with the iridium center or with another hydride coordinated to the center. Which of the later is chosen depends on which proposed outer sphere mechanism is followed.

Acknowledgements

I performed this project at the Inorganic System Engineering group at the Delft University of Technology to obtain the degree of Bachelor of Science. It was a fun project to work on in the company of friendly people who are more than happy to help each other out. What stood out to me is the open atmosphere which made it easy to feel welcome in the group. My daily supervisor Adarsh Kalikadien came up with the idea of trying out dishes from different cultural backgrounds for lunch on Fridays. I enjoyed these lunches very much. I have never had Surinamese food before, which was actually quite good. Also the tortillas made by Hector were very tasty.

I would like to thank some people who helped me during this project. I want to start by thanking Professor Evgeny Pidko. He welcomed me with open arms in the group and was very enthusiastic about my research from the start. I think your enthusiasm is contagious because after the first online meeting, I also became very excited about the project. I would like to thank you for your guidance during this project and for answering all my questions, even during the weekend. Even though you have a busy schedule, you found the time to help me out and show me the next steps for my research.

Furthermore, I would like to thank my daily supervisor Adarsh Kalikadien. You showed me how to use Linux and how to submit jobs on Snellius. What I appreciate is that you explained your actions when changing the settings in Linux. In that way, got some understanding about how that program works. Computational wise, I learned a lot from you. I would also like to thank you for answering my questions and helping me out when I got for example error terminations of jobs.

I am thankful for the bachelor and PhD students with whom I could exchange ideas. Elena Khramenkova helped me get along with adobe illustrator, which would have cost me a lot of time if I had to figure that out on my own. You also took the time to look at the results with me, which I appreciated very much. Moreover, I want to thank Wenjun Yang for looking at the outer sphere mechanism with me. And last but not least, I want to thank bachelor student Mark Heezen. Most of the time we worked beside each other in the office which was always very enjoyable. We could share a laugh and still work hard. I could always come to you with my (sometimes laughable) questions about computers and their settings. So thank you for that.

- Britt van Dongen
Delft, June 2022

Bibliography

[1] M. Gouygou, P. Kalck, and M. Urrutigoïty. Enantioselective hydrogenation of CC and CX bonds. In *Comprehensive Inorganic Chemistry II*, pages 223–247. Elsevier, 2013. doi: 10.1016/b978-0-08-097774-4.00611-2. URL https://doi.org/10.1016/b978-0-08-097774-4.00611-2.

[2] Xumu Zhang, Yongxiang Chi, and Wenjun Tang. C–h bond formation by asymmetric and stereoselective hydrogenation. In *Comprehensive Organometallic Chemistry III*, pages 1–70. Elsevier, 2007. doi: 10.1016/b0-08-045047-4/00123-0. URL https://doi.org/10.1016/b0-08-045047-4/00123-0.

[3] James T Richardson. *Principles of catalyst development*. Springer, 2013.

[4] Piet WNM Van Leeuwen. *Homogeneous catalysis: understanding the art*. Springer Science & Business Media, 2006.

[5] Ulf Hanefeld and Leon Lefferts. *Catalysis: an integrated textbook for students*. John Wiley & Sons, 2018.

[6] Brandon Tutkowski, Sutthichat Kerdphon, Elaine Limé, Paul Helquist, Pher G. Andersson, Olaf Wiest, and Per-Ola Norrby. Revisiting the stereodetermining step in enantioselective iridium-catalyzed imine hydrogenation. *ACS Catalysis*, 8(1):615–623, December 2017. doi: 10.1021/acscatal.7b02386. URL https://doi.org/10.1021/acscatal.7b02386.

[7] Nicolas Fleury-Brégeot, Verónica de la Fuente, Sergio Castillón, and Carmen Claver. Highlights of transition metal-catalyzed asymmetric hydrogenation of imines. *ChemCatChem*, 2(11):1346–1371, August 2010. doi: 10.1002/cctc.201000078. URL https://doi.org/10.1002/cctc.201000078.

[8] Kathrin Helen Hopmann and Annette Bayer. Enantioselective imine hydrogenation with iridium-catalysts: Reactions, mechanisms and stereocontrol. *Coordination Chemistry Reviews*, 268:59–82, June 2014. doi: 10.1016/j.ccr.2014.01.023. URL https://doi.org/10.1016/j.ccr.2014.01.023.

[9] Silas W. Smith. Chiral toxicology: It's the same thing... only different. *Toxicological Sciences*, 110(1):4–30, May 2009. doi: 10.1093/toxsci/kfp097. URL https://doi.org/10.1093/toxsci/kfp097.

[10] Annika M. Krieger and Evgeny A. Pidko. The impact of computational uncertainties on the enantioselectivity predictions: A microkinetic modeling of ketone transfer hydrogenation with a noyori-type mn-diamine catalyst. *ChemCatChem*, 13(15):3517–3524, June 2021. doi: 10.1002/cctc.202100341. URL https://doi.org/10.1002/cctc.202100341.

[11] Andrew K. Scott. Stereoisomers and drug toxicity. *Drug Safety*, 8(2):149–159, February 1993. doi: 10.2165/00002018-199308020-00005. URL https://doi.org/10.2165/00002018-199308020-00005.

[12] Ho Ryu, Jiyong Park, Hong Ki Kim, Ji Young Park, Seoung-Tae Kim, and Mu-Hyun Baik. Pitfalls in computational modeling of chemical reactions and how to avoid them. *Organometallics*, 37(19):3228–3239, September 2018. doi: 10.1021/acs.organomet.8b00456. URL https://doi.org/10.1021/acs.organomet.8b00456.

[13] Christoph Bannwarth, Eike Caldeweyher, Sebastian Ehlert, Andreas Hansen, Philipp Pracht, Jakob Seibert, Sebastian Spicher, and Stefan Grimme. Extended scptight-binding/scp quantum chemistry methods. *WIREs Computational Molecular Science*, 11(2), August 2020. doi: 10.1002/wcms.1493. URL https://doi.org/10.1002/wcms.1493.

[14] Maylis Orio, Dimitrios A. Pantazis, and Frank Neese. Density functional theory. *Photosynthesis Research*, 102(2-3):443–453, February 2009. doi: 10.1007/s11120-009-9404-8. URL https://doi.org/10.1007/s11120-009-9404-8.

[15] P. Geerlings, F. De Proft, and W. Langenaeker. Conceptual density functional theory. *Chemical Reviews*, 103(5):1793–1874, April 2003. doi: 10.1021/cr990029p. URL https://doi.org/10.1021/cr990029p.

[16] LIU Shu-Bin and and. Conceptual density functional theory and some recent developments. *Acta Physico-Chimica Sinica*, 25(03):590–600, 2009. doi: 10.3866/pku.whxb20090332. URL https://doi.org/10.3866/pku.whxb20090332.

[17] Aron J. Cohen, Paula Mori-Sánchez, and Weitao Yang. Challenges for density functional theory. *Chemical Reviews*, 112(1):289–320, December 2011. doi: 10.1021/cr200107z. URL https://doi.org/10.1021/cr200107z.

[18] Adarsh Kalikadien. Automated data-driven exploration of chemical space for catalysts. Master's thesis, Delft University of Technology, April 2021.

[19] Vivek Sinha. *The molecular basis of clean energy*. PhD thesis, University of Amsterdam, 2019. URL https://dare.uva.nl/search?identifier=ff73daec-b6f3-4a5f-b2b4-c85261131fce.

[20] Roberto Peverati and Donald G. Truhlar. Exchange–correlation functional with good accuracy for both structural and energetic properties while depending only on the density and its gradient. *Journal of Chemical Theory and Computation*, 8(7):2310–2319, June 2012. doi: 10.1021/ct3002656. URL https://doi.org/10.1021/ct3002656.

[21] Kieron Burke. Perspective on density functional theory. *The Journal of Chemical Physics*, 136(15):150901, April 2012. doi: 10.1063/1.4704546. URL https://doi.org/10.1063/1.4704546.

[22] Stig Rune Jensen, Tor Flå, Dan Jonsson, Rune Sørland Monstad, Kenneth Ruud, and Luca Frediani. Magnetic properties with multiwavelets and DFT: the complete basis set limit achieved. *Physical Chemistry Chemical Physics*, 18(31):21145–21161, 2016. doi: 10.1039/c6cp01294a. URL https://doi.org/10.1039/c6cp01294a.

[23] Basis sets. In *Computational Chemistry and Molecular Modeling*, pages 115–138. Springer Berlin Heidelberg. doi: 10.1007/978-3-540-77304-7_6. URL https://doi.org/10.1007/978-3-540-77304-7_6.

[24] Florian Weigend and Reinhart Ahlrichs. Balanced basis sets of split valence, triple zeta valence and quadruple zeta valence quality for h to rn: Design and assessment of accuracy. *Physical Chemistry Chemical Physics*, 7(18):3297, 2005. doi: 10.1039/b508541a. URL https://doi.org/10.1039/b508541a.

[25] Jin Zhang, Haiyang Zhang, Tao Wu, Qi Wang, and David van der Spoel. Comparison of implicit and explicit solvent models for the calculation of solvation free energy in organic solvents. *Journal of Chemical Theory and Computation*, 13(3):1034–1043, March 2017. doi: 10.1021/acs.jctc.7b00169. URL https://doi.org/10.1021/acs.jctc.7b00169.

[26] What is dichloromethane. https://www.chemicals.co.uk/blog/what-is-dichloromethane. Accessed: 2022-05-23.

[27] Stefan Grimme, Stephan Ehrlich, and Lars Goerigk. Effect of the damping function in dispersion corrected density functional theory. *Journal of Computational Chemistry*, 32(7):1456–1465, March 2011. doi: 10.1002/jcc.21759. URL https://doi.org/10.1002/jcc.21759.

[28] Esra Boz and Matthias Stein. Accurate receptor-ligand binding free energies from fast QM conformational chemical space sampling. *International Journal of Molecular Sciences*, 22(6):3078, March 2021. doi: 10.3390/ijms22063078. URL https://doi.org/10.3390/ijms22063078.

[29] Stefan Grimme. Exploration of chemical compound, conformer, and reaction space with metadynamics simulations based on tight-binding quantum chemical calculations. *Journal of Chemical Theory and Computation*, 15(5):2847–2862, April 2019. doi: 10.1021/acs.jctc.9b00143. URL https://doi.org/10.1021/acs.jctc.9b00143.

[30] Philipp Pracht, Fabian Bohle, and Stefan Grimme. Automated exploration of the low-energy chemical space with fast quantum chemical methods. *Physical Chemistry Chemical Physics*, 22(14):7169–7192, 2020. doi: 10.1039/c9cp06869d. URL https://doi.org/10.1039/c9cp06869d.

[31] Anna Theresa Cavasin, Alexander Hillisch, Felix Uellendahl, Sebastian Schneckener, and Andreas H. Göller. Reliable and performant identification of low-energy conformers in the gas phase and water. *Journal of Chemical Information and Modeling*, 58(5):1005–1020, May 2018. doi: 10.1021/acs.jcim.8b00151. URL https://doi.org/10.1021/acs.jcim.8b00151.

[32] Dmitry I. Sharapa, Alexander Genaev, Luigi Cavallo, and Yury Minenkov. A robust and cost-efficient scheme for accurate conformational energies of organic molecules. *ChemPhysChem*, December 2018. doi: 10.1002/cphc.201801063. URL https://doi.org/10.1002/cphc.201801063.

[33] Stefan Grimme, Christoph Bannwarth, and Philip Shushkov. A robust and accurate tight-binding quantum chemical method for structures, vibrational frequencies, and noncovalent interactions of large molecular systems parametrized for all spd-block elements (iz/i = 1–86). *Journal of Chemical Theory and Computation*, 13(5):1989–2009, April 2017. doi: 10.1021/acs.jctc.7b00118. URL https://doi.org/10.1021/acs.jctc.7b00118.

[34] Christoph Bannwarth, Sebastian Ehlert, and Stefan Grimme. GFN2-xTB—an accurate and broadly parametrized self-consistent tight-binding quantum chemical method with multipole electrostatics and density-dependent dispersion contributions. *Journal of Chemical Theory and Computation*, 15(3):1652–1671, February 2019. doi: 10.1021/acs.jctc.8b01176. URL https://doi.org/10.1021/acs.jctc.8b01176.

[35] Markus Bursch, Hagen Neugebauer, and Stefan Grimme. Structure optimisation of large transition-metal complexes with extended tight-binding methods. *Angewandte Chemie International Edition*, 58 (32):11078–11087, August 2019. doi: 10.1002/anie.201904021. URL https://doi.org/10.1002/anie.201904021.

[36] Grimme group Revision. Example applications kernel description. https://xtb-docs.readthedocs.io/en/latest/crestxmpl.html#constrained-conformational-sampling. Accessed: 2022-05-22.

[37] Karen Sargsyan, Cédric Grauffel, and Carmay Lim. How molecular size impacts RMSD applications in molecular dynamics simulations. *Journal of Chemical Theory and Computation*, 13(4):1518–1524, March 2017. doi: 10.1021/acs.jctc.7b00028. URL https://doi.org/10.1021/acs.jctc.7b00028.

[38] Evangelos A. Coutsias, Chaok Seok, and Ken A. Dill. Using quaternions to calculate RMSD. *Journal of Computational Chemistry*, 25(15):1849–1857, 2004. doi: 10.1002/jcc.20110. URL https://doi.org/10.1002/jcc.20110.

[39] Chemcraft. Structures comparer window. https://www.chemcraftprog.com/help/structcomparerwindow.html.

[40] Andrea Hamza, Daniel Moock, Christoph Schlepphorst, Jacob Schneidewind, Wolfgang Baumann, and Frank Glorius. Unveiling a key catalytic pocket for the ruthenium NHC-catalysed asymmetric heteroarene hydrogenation. *Chemical Science*, 13(4):985–995, 2022. doi: 10.1039/d1sc06409f. URL https://doi.org/10.1039/d1sc06409f.

[41] Vivek Sinha, Jochem J. Laan, and Evgeny A. Pidko. Accurate and rapid prediction of pik/isuba/sub of transition metal complexes: semiempirical quantum chemistry with a data-augmented approach. *Physical Chemistry Chemical Physics*, 23(4):2557–2567, 2021. doi: 10.1039/d0cp05281g. URL https://doi.org/10.1039/d0cp05281g.

A

Inner sphere C-migration mechanism: supporting information

E = Electronic Energy
ZPE = Zero-Point Energy
H = Thermal Enthalpy
G = Thermal Gibbs Free Energy

Species	E (Hartree)	ZPE (Hartree)	H (Hartree)	G (Hartree)
H_2	-1.160986912	0.00995	-1.147733	-1.162578
2-Methyl-1-pyrroline	-2.502067762	0.133527	-2.50066304	-2.5010261

Figure A.1: DFT calculated data for the free molecules of the inner sphere C-migration mechanism.

Species	E (Hartree)	ZPE (Hartree)	H (Hartree)	G (Hartree)
Complex 1_1	-3294.150408	0.68358	-3293.427677	-3293.533159
Complex 1_2	-3294.148931	0.683749	-3293.426151	-3293.53176
Complex 1_3	-3294.139115	0.682177	-3293.418034	-3293.523208
Complex 1_4	-3294.139156	0.682212	-3293.418092	-3293.523073
Complex $2_{1S/1R}$	-3543.20419	0.804564	-3542.354793	-3542.473151
Complex 2_{2S}	-3543.213855	0.804271	-3542.364397	-3542.483575
Complex $2_{3S/3R1}$	-3543.212101	0.802747	-3542.364302	-3542.482423
Complex 2_{3R2}	-3543.212388	0.803284	-3542.364089	-3542.482096
Complex$2_{4S/4R1}$	-3543.203633	0.80272	-3542.355703	-3542.475788
Complex $2_{4R2/4R3}$	-3543.204054	0.802868	-3542.356102	-3542.474847
Complex $3_{a,1S}$	-3543.211479	0.804841	-3542.361617	-3542.480366
Complex $3_{a,1R}$	-3543.212377	0.804558	-3542.362847	-3542.481092
Complex $3_{a,2S}$	-3543.21648	0.804581	-3542.366997	-3542.484696
Complex $3_{a,3S}$	-3543.212101	0.802755	-3542.364298	-3542.482395
Complex $3_{a,3R1}$	-3543.211771	0.803054	-3542.363668	-3542.482019
Complex $3_{b,3R2}$	-3543.180086	0.803124	-3542.332253	-3542.449335
Complex $3_{a,4S}$	-3543.203633	0.80272	-3542.355703	-3542.475777
Complex $3_{a,4R1}$	-3543.203633	0.802728	-3542.355698	-3542.475768
Complex $3_{b,4R2}$	-3543.173393	0.803595	-3542.325201	-3542.442142
Complex $3_{a,4R3}$	-3543.204054	0.802869	-3542.356101	-3542.47484
Complex 4_{1S}	-3543.166995	0.804692	-3542.317788	-3542.434218
Complex 4_{1R}	-3543.162807	0.804953	-3542.313412	-3542.429617
Complex 4_{2S}	-3543.156055	0.805137	-3542.306631	-3542.422098
Complex 4_{3S}	-3543.172934	0.803678	-3542.324877	-3542.441574
Complex 4_{3R1}	-3543.176499	0.805905	-3542.325939	-3542.443903
Complex 4_{3R2}	-3543.182051	0.80542	-3542.331985	-3542.44942
Complex 4_{4S}	-3543.171303	0.804392	-3542.322821	-3542.438437
Complex 4_{4R1}	-3543.17913	0.807443	-3542.326929	-3542.445477
Complex 4_{4R2}	-3543.178107	0.805908	-3542.327505	-3542.445834
Complex 4_{4R3}	-3543.164832	0.804845	-3542.315837	-3542.432165
Complex 5_{1S}	-3544.345882	0.823434	-3543.477108	-3543.595068
Complex 5_{1R}	-3544.341979	0.823114	-3543.473375	-3543.591509
Complex 5_{2S}	-3544.34923	0.823314	-3543.480559	-3543.598022
Complex 5_{3S}	-3544.352116	0.822433	-3543.484585	-3543.60174
Complex 5_{3R1}	-3544.358625	0.823557	-3543.489478	-3543.60923
Complex 5_{3R2}	-3544.358083	0.823578	-3543.489	-3543.608579
Complex 5_{4S}	-3544.343487	0.822399	-3543.475945	-3543.594515
Complex 5_{4R1}	-3544.354977	0.823544	-3543.485864	-3543.606041
Complex 5_{4R2}	-3544.35822	0.823808	-3543.489133	-3543.608205
Complex 5_{4R3}	-3544.360399	0.824149	-3543.490959	-3543.610073

Figure A.2: DFT calculated data for the intermediates of the inner sphere C-migration mechanism.

Species	E (Hartree)	ZPE (Hartree)	H (Hartree)	G (Hartree)
$TS_{3->4,1S}$	-3543.166904	0.803478	-3542.31939	-3542.434626
$TS_{3->4,1R}$	-3543.16168	0.802468	-3542.314859	-3542.430959
$TS_{3->4,2S}$	-3543.154967	0.803186	-3542.30778	-3542.422386
$TS_{3->4,3S}$	-3543.171564	0.801366	-3542.326006	-3542.442347
$TS_{3->4,3R1}$	-3543.165446	0.802154	-3542.31904	-3542.434898
$TS_{3->4,3R2}$	-3543.173464	0.802539	-3542.32686	-3542.441801
$TS_{3->4,4S}$	-3543.169796	0.801718	-3542.324003	-3542.439655
$TS_{3->4,4R1}$	-3543.139535	0.802118	-3542.292992	-3542.409767
$TS_{3->4,4R2}$	-3543.166217	0.802214	-3542.319666	-3542.436042
$TS_{3->4,4R3}$	-3543.161369	0.801643	-3542.315533	-3542.431749

Figure A.3: DFT calculated data for the transition states of the inner sphere C-migration mechanism.

Species	E (Hartree)	ZPE (Hartree)	H (Hartree)	G (Hartree)
$TS_{3S,CREST}$	-3543.169085	0.801243	-3542.323516	-3542.440496
$TS_{3R1,CREST}$	-3543.164406	0.802857	-3542.317246	-3542.433458
$TS_{3R2,CREST}$	-3543.176899	0.804856	-3542.327771	-3542.445219
$TS_{3S,DFT}$	-3543.171564	0.801366	-3542.326006	-3542.442347
$TS_{3R1,DFT}$	-3543.165446	0.802154	-3542.31904	-3542.434898
$TS_{3R2,DFT}$	-3543.173464	0.802539	-3542.32686	-3542.441801

Figure A.4: DFT and GFNn-xTB with CREST calculated data for the transition states of the inner sphere C-migration mechanism of path 3S, $3R_1$ and $3R_2$.

B

Inner sphere C-migration mechanism: structures of the complexes for each investigated path

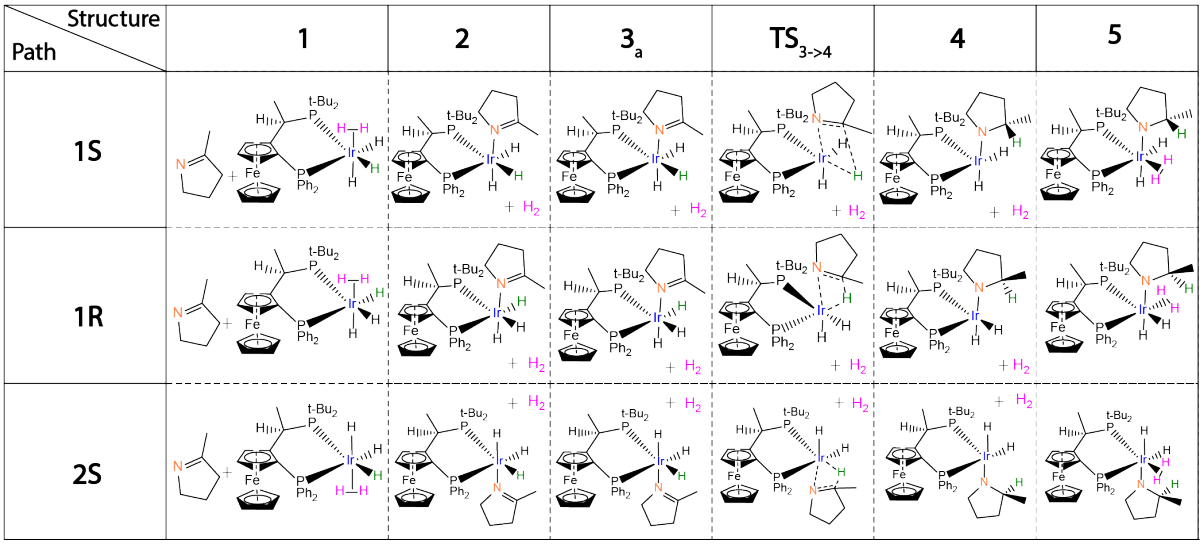

Figure B.1: Structures of the complexes for the 1S, 1R and 2S paths. The hydride which reacts with the substrate is colored green.

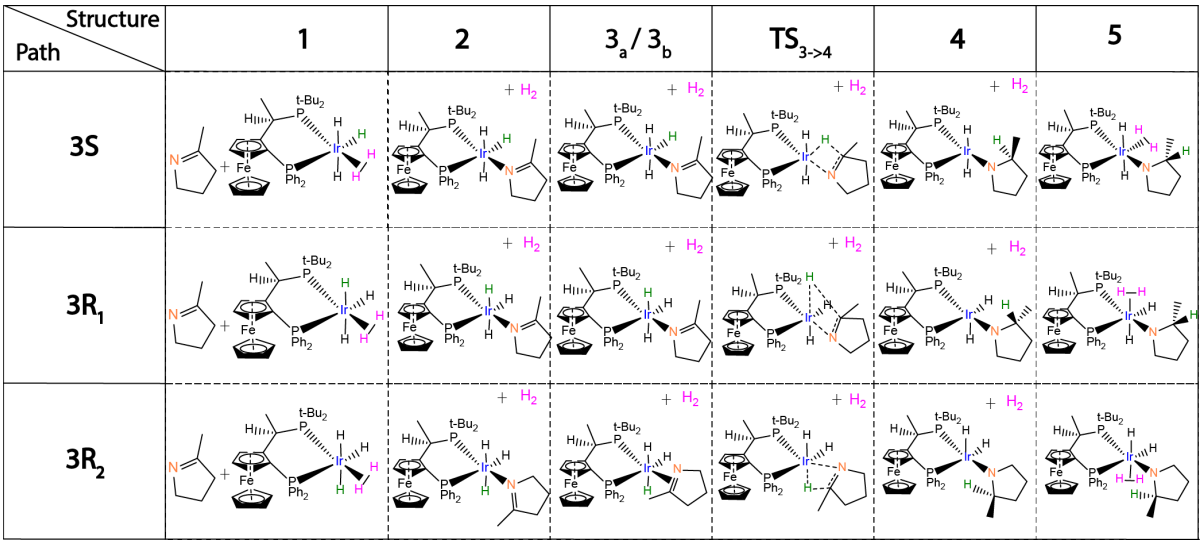

Figure B.2: Structures of the complexes for the 3S, $3R_1$ and $3R_2$ paths. The hydride which reacts with the substrate is colored green.

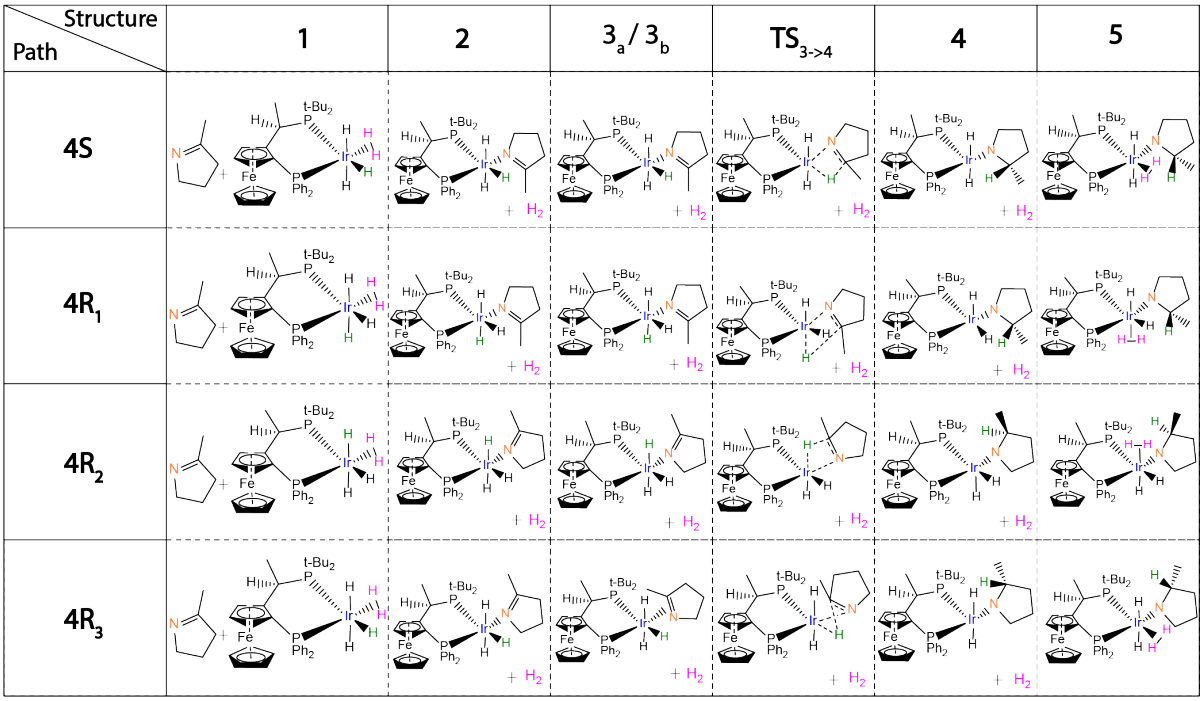

Figure B.3: Structures of the complexes for the 4S, $4R_1$, $4R_2$ and $4R_3$ paths. The hydride which reacts with the substrate is colored green.

C

Outer sphere mechanism: supporting information

E = Electronic Energy
ZPE = Zero-Point Energy
H = Thermal Enthalpy
G = Thermal Gibbs Free Energy

Species	E (Hartree)	ZPE (Hartree)	H (Hartree)	G (Hartree)
Complex 1_3	-3294.139115	0.682177	-3293.41803	-3293.52321
Complex 6	-3544.348348	0.822846	-3543.48049	-3543.59713
$TS_{6->7}$	-3544.329699	0.820775	-3543.46378	-3543.5811
Complex 7	-3544.363842	0.825465	-3543.49259	-3543.61329

Figure C.1: DFT calculated data for the complexes of the outer sphere mechanism.

D

Outer sphere mechanism: structures of the complexes for each investigated path

Path \ Structure	1	6	$TS_{6->7}$	7
$3S_2$	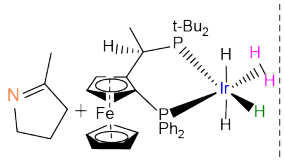	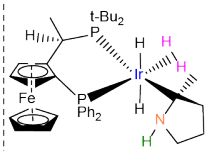	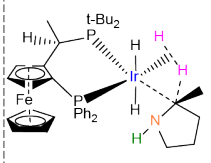	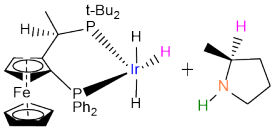

Figure D.1: Structures of the complexes for the 3S2 and 3R3 paths.